Numerical and Experimental Study of an Aircraft Igniter Plasma Jet Discharge

Yihao Tang^{1,2,3} *, Joohan Kim¹ †, Brandon Sforzo¹ ‡, Riccardo Scarcelli¹ §, and Venkat Raman² ¶

¹ Argonne National Laboratory, Lemont, IL 60439, USA

² University of Michigan, Ann Arbor, MI 48109, USA

³ Beihang University, Beijing, 100191, China

The spark discharge of an aircraft plasma jet igniter is studied using high-fidelity numerical simulations and X-ray radiography measurements. The target problem here features the thermal expansion of hot gas introduced by the electric spark within a confined igniter cavity, which eventually evolves into a pulsed jet of a high-temperature kernel. A comprehensive set of models adapted from existing strategies for ICE spark plug discharge is extended to the target problem, including the modeling of energy deposition, plasma reactions, thermodynamic properties, and heat losses. A series of validation and parameter studies are performed and presented. The kernel size is found to be sensitive to heat losses arising from radiation and hot gas remained within the discharge cavity, rather than heat conduction to the wall in the discharge cavity. Depending on the enforced shape of the post-breakdown electric arc, the spark kernel can be off-centered, tilted, and considerably asymmetric. These features have been previously not considered when studying such igniter configurations and may have a first-order impact on the ignition process. Provided a proper set-up of the heat loss models and electric arc shape, the numerical results are quantitatively comparable to the experimental results in terms of the kernel size, shape, and velocity throughout different stages after the spark discharge.

I. Introduction

Modern aircraft use electric-spark-based ignition of combustors. The major design focus of the spark igniter is in ensuring longevity and maintenance accessibility of the device [1]. However, the early stage kernel development from an igniter discharge can have a large impact on ensuring successful ignition, which can be critical for high-altitude relight [2]. In this context, a comprehensive understanding of the early stage kernel evolution following an aircraft spark igniter discharge is needed.

^{*}Graduate Research Aide, Energy System Division; yhtang@umich.edu.

[†]Research Scientist, Energy System Division.

[‡]Research Engineer, Energy System Division. Senior Member AIAA.

[§]Principal Research Scientist, Energy System Division.

[¶]Professor, Aerospace Engineering. Associate Fellow AIAA.

Previously, the spark discharge mechanism and the subsequent kernel evolution have been extensively studied in the context of internal combustion engines (ICEs) [3-17]. In ICE discharge, the focus is on understanding the heat loss during spark discharge that leads to discrepancies between the theoretical and measured minimum ignition energy (MIE) [3, 4]. In particular, Maly and Vogel [6] conducted a comprehensive series of experimental studies of electric spark discharge in CH₄/air mixture and quantified the energy deposition efficiency of different phases of the ignition spark. Sher et al. [7] carried out a 0-d theoretical analysis of the breakdown stage of a spark discharge in air and found the resulting kernel temperature after the initial kernel expansion to be sensitive to the thermodynamic modeling. Later, following studies [8–13] started leveraging direct numerical simulations (DNS) to explore the kernel evolutions at the incipient stages. Kono et al. [8] studied the short-duration spark discharge in pure nitrogen in a pin-to-pin electrode configuration and found the kernel vortexes are suppressed in the vertical (pin-to-pin) direction, which causes the initially elliptic shape kernel to expand in a torus fashion. Kravchik et al. [9] simulated the spark discharge and flame propagation in an ICE and found the spark kernel growth can be described as two stages of an early stage dominated by the pressure wave and a later stage where the contribution of chemical reactions becomes sensible, which is consistent to the numerical results of Thiele et al. [11] using a similar configuration. Kravchik et al. [9] further identified factors related to the spark discharge (e.g., power profile, electrode diameters, ...) that can be controlled to enhance the kernel growth via a parameter study. Among those DNS studies, except for Ref. [8] and [13], all the others have applied high-fidelity modeling to couple the electric spark discharge with the fluid dynamics, i.e., as a spatial-temporal energy source formulated by the joule heating law, where the electric current is determined either by experimental measurements [9] or by solving the electric potential equation [11, 12]. Besides, many of those studies include detailed modeling descriptions of the dissociation and ionization of the spark-induced plasma [9, 11–13] as well as the high-temperature gas thermodynamic properties [9, 10, 13]. In more recent studies of practical ignition problems using Reynolds-averaged numerical simulation (RANS) and large-eddy simulation (LES), where high-fidelity modeling of the early spark discharge is computationally infeasible, spark ignition models [14–17] were developed for the under-resolved spark discharge physics. The Arc and Kernel Tracking Ignition Model (AKTIM) [15], which was first proposed for RANS simulation and later extended to LES simulations [18], applies Lagrangian particles to track the electric arc during the spark discharge, and applies semi-empirical correlations to estimate the amount of energy deposited into the gas phase. A recently proposed Lagrangian-Eulerian Spark-Ignition (LESI) model [17] has further improved the particle tracking/representation of the electric arc to better capture the arc elongation effects during the discharge. In these spark ignition models, the plasma reactions and the thermodynamic properties are often modelled with certain simplifications. For instance, the ionization reactions are often neglected [14, 15, 18], and the thermodynamic properties of the high-energy kernel are extrapolated from the combustion burnt gas assuming constant heat capacity [15]. Despite sacrificing part of the modeling fidelity, these spark ignition models are generally implementation friendly and compatible with existing combustion models and have been widely adopted by the latest

studies [19, 20].

While the abundant previous studies of ICE ignitions can provide insights into the spark discharge in aircraft gas turbine combustors, there are large discrepancies between an aircraft spark igniter and an ICE spark plug. Specifically, ICE spark plugs often apply a center cathode on top and an L-shaped anode on the bottom that are directly exposed to the outer flow, which is a relatively simple geometry that leads to a spherical flame kernel that expands mostly in the radial direction with mild asymmetry [21]. Aircraft igniters, however, often feature a more complicated geometry. Some of the commonly applied aircraft igniter layouts include the flash fire surface discharge igniter [1], the sunken fire igniter (or the surface gap igniter) [1, 22], the pulsed plasma jet igniter [23, 24]. Among those layouts, many feature an electric spark taking place within a confined cavity and the kernel being ejected from a gap on the igniter outer surface due to the spark-induced thermal expansion. The fluid dynamics of the resulting kernel characterize a pulsing jet moving away from the igniter tip, which can further interact with the cross-flow and critically affects the downstream ignition process via fuel mixing and energy dissipation [25–27]. Therefore, the important physics here is not only the energy conversion, the kernel size growth, but also the penetration and vortex dynamics of the pulsing kernel, which is challenging to predict, as the detailed information inside the igniter cavity cannot be accurately measured. Besides, the energy conversion here can also be vastly different from an ICE engine spark plug, where the nominal electrical energy of an aircraft igniter discharge (1 - 10 J) is often orders of magnitudes larger than an ICE engine spark plug (< 150 mJ), which should lead to stronger dissociation reactions and radiation.

Previous studies [23, 28–33] of aircraft spark igniter discharge have nonetheless achieved several findings. Early studies were focusing on identifying the dominating physics of the kernel pulsing. Bradley and Critchley [28] studied the kernel motion of flush fire surface discharge igniter and found the electromagnetic force in certain scenarios playing an important role in expelling the kernel. However, a later study of Clements et al. [23] confronted this idea, concluding that the dominating factor that contributes to the kernel momentum is still due to the pressure wave instead of electromagnetic forces. Cetegen et al. [29] performed an analytical study of pulsed plasma jet igniter and predicted the kernel penetration depth to be proportional to the igniter characteristic length, i.e., the ratio of igniter cavity to orifice area. Those early studies showed the importance of including compressibility effects and a proper thermodynamic model to accurately capture the kernel pulsing. Later studies tried to characterize the extent of the kernel by different experimental measurement techniques [30, 31, 33]. In particular, Okhovat [31] applied radiation intensity measurement to determine the kernel temperature. By assuming an oval shape of the kernel, Okhovat provided a quantitative estimation of the kernel sensible enthalpy (0.6 J), which is only a small fraction of the nominal electric energy (10 J). Recently, Sforzo et al. [33] applied X-ray radiography to measure the pulsing kernel emerged from a pulsed plasma jet igniter discharge, which is one of the few efforts that accurately measured the size, trajectory, and energy of a spark kernel. Similar to Ref. [31], Sforzo et al. [33] also found the energy of the pulsing kernel (0.2 J) to be a small fraction of the nominal spark energy (1.24 J).

Despite the above-mentioned efforts, the topic of aircraft spark igniter discharge is understudied. In particular, previous efforts were predominating experimental and theoretical, while numerical studies can rarely be found. A basic understanding of the modeling strategies to directly simulate a spark discharge is lacking. This poses further challenges to the kernel initialization in aircraft combustor forced ignition simulations, which in many cases end up being simplified to pure energy deposition without resolving the igniter geometry [34] or flow patching using burnt product conditions [35, 36]. In some studies, a more accurate method using enforced velocity profile at the igniter tip was applied to reproduce the kernel pulsing [2, 25, 37–40]. However, such a strategy relies on calibration against experimental data of the kernel shape and trajectory which is not always available.

Based on the above, an understanding study of numerically predicting the early stage kernel evolution of aircraft igniter discharge is carried out here. The same pulsed plasma jet igniter configuration studied by Sforzo *et al.* [33] is investigated, using high-fidelity LES simulation with compressible pressure-velocity coupling to capture the thermal expansion effect that expels the kernel. A parametric study is performed to determine the key modeling features and uncertainties. The numerical results are analyzed to provide insight into the energy loss mechanism of the spark kernel. The remaining of this manuscript is as follows: in Section II, the target configuration and the interpretation of experimental data are explained; in Section III, the applied modeling strategies of the target plasma jet igniter discharge are explained in detail and validated using multiple canonical problems; in Section IV, the applied CFD solver, as well as post-processing techniques, are introduced; in Section V, the results are presented and analyzed in terms of studying the impact of different modeling components and parameter setups and understanding the physics of kernel expansion and pulsing; and conclusions are provided in the end.

II. Experimental Configuration

A commercial aircraft igniter is investigated in this study, which is tested in the simple operating condition of quiescent pure air. The available experimental data is obtained using X-ray radiography measurements. More details of the configuration and interpretation of the X-ray data are provided in the following two subsections.

A. Commercial pulsed plasma jet igniter

The geometry here is axial-symmetric. A schematic is shown in Fig. 1 at a cross-section through the geometry center. The target igniter is a commercial aircraft igniter designed by the original equipment manufacture (OEM) and adopts the configuration of a pulsed plasma jet igniter, which is one of the several popular igniter configurations introduced in Sec. I. The feature of the sunken fire igniter is that the central cathode, outer anode, and the spark gap in between constitute a confined region, referred to here as the "igniter cavity", where the electric spark takes place. In contrary to the flush fire igniter where the kernel is allowed to expand freely, here, the spark discharge takes place within this relatively confined environment. This introduces a prominent thermal expansion that expels the kernel from the

igniter cavity and eventually yields an upwardly pulsing kernel. It is clarified that the layout shown in Fig. 1 is simply demonstrative, whereas the precise details including the dimensionalities are intellectual properties and not necessarily the same as in the schematic. Nonetheless, a series of parameter studies have been conducted in the preliminary stage of this study and found that, within the uncertainties of 2 mm, the simulation results are insensitive to the lack of understandings of those details.

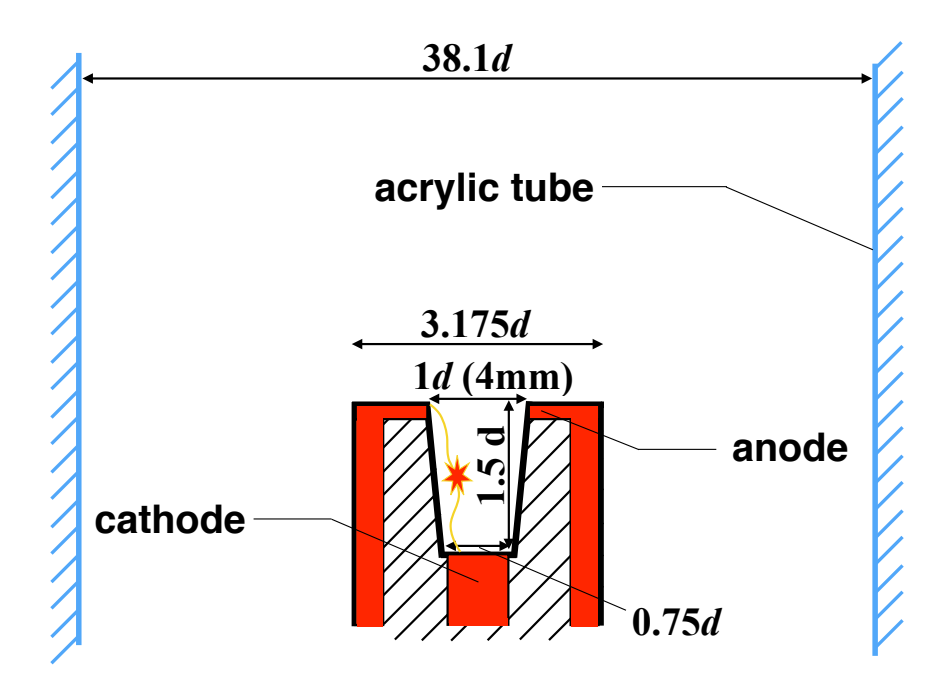


Fig. 1 Schematic of the experimental configuration. Internal size and layouts are demonstrative only and do not present actual details.

The above configuration is studied under atmospheric conditions. Under practical conditions, the background pressure and temperature within the combustor will be different. However, due to the large spark-induced pressure and temperature rise compared to these background conditions, it is expected that the physical processes will remain the same.

B. X-ray diagnostic of pulsing kernel

The X-ray diagnostic techniques applied in the experimental study [33] are explained here for a better understanding of the experimental data. Due to the strong electromagnetic interference and light emission of the aircraft igniter discharge, visualization techniques using shadowgraph or schlieren [13], and more specifically, density gradients in

reacting flows [30], while commonly used to characterize the extent of spark kernels on the millisecond timescale, are inapplicable to measure the kernel status shortly after the discharge on the microsecond timescale. The X-ray beam is much less sensitive to scattering and can thus provide quantitative data inside optically incompatible flow fields. One feature of the X-ray measurement is that each measurement is a line-of-sight (LOS) probe of the gas field taken at a fixed incident point. Therefore, it is impossible to record the entire spatial distribution of the kernel property from a single spark discharge sequence using the X-ray beam. Instead, the spatial distribution is reconstructed on a raster grid (see bottom left of Fig. 2) of a total of 4000 measurement points, where the time sequence of the spark discharge is recorded in the *x*, *y*-directions, each point at a time. Further, to reduce the shot-to-shot uncertainties, the time histories at each point are measured as the ensemble average of multiple realizations of the spark discharge sequences. Therefore, the X-ray dataset does not depict the kernel evolution in any *single* discharge sequence, but instead the *ensemble* kernel behavior following the spark discharge. More details are further explained below.

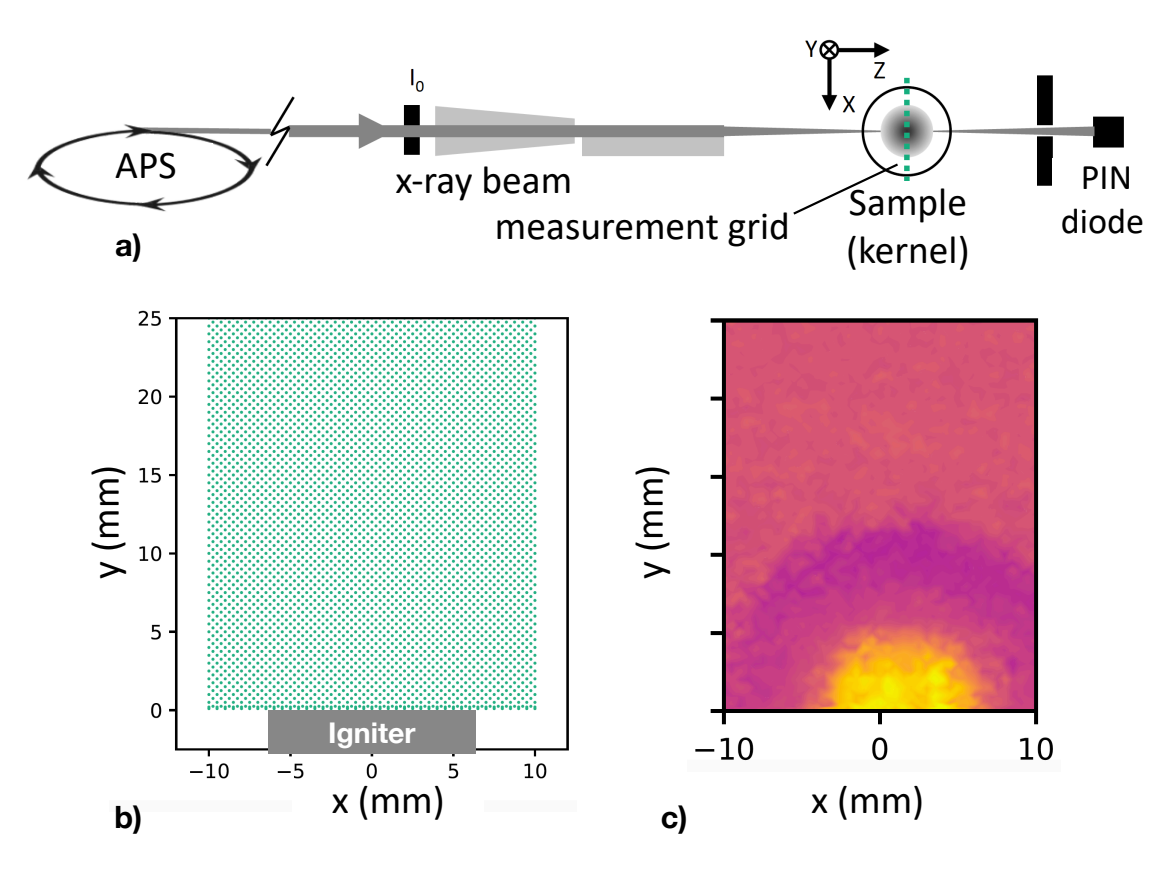


Fig. 2 Illustration of X-ray diagnostics of kernel status, reproduced from Ref. [33]. a) Top view of the X-ray radiography layout. b) Raster grid of experimental measurements. c) Measured gas displacement contour.

The direct output of each X-ray measurement is the decay of the light intensity of the X-ray beam along its pathway,

which is then converted to gas displacement using the Beer-Lambert law [41], as

$$L(x, y, t) = \int_0^1 \frac{\rho_0 - \rho(z)}{\rho_0} dz = -\frac{1}{\mu \rho_0} \ln \frac{I_0(x, y)}{I(x, y, t)}.$$
 (1)

Here, L is the gas displacement, μ is the photoelectric absorption coefficient, which applies a constant value in Ref. [33], I is the measured beam intensities, and ρ is the density. The subscript 0 denotes the baseline value measured from the ambient gas without the presence of the kernel. The gas displacement L is a critical property that reveals the size, shape, and trajectory of the kernel. By the mathematical definition, L is dependent on the LOS integration of density variation induced by the kernel. Physically, L > 0 means gas expansion, L < 0 means compression, and in the most extreme condition where the hot gas density approaches zero, L approaches the length of the vacuum space occupied by the kernel in the LOS direction. In this context, L is a point-wise measurement of the kernel width in the LOS direction.

In the experimental study [33], L is reconstructed as a time series of 2-D contours on the experimental measurement grid to visualize the kernel. To obtain the L-contour, firstly, as explained above, the time history of L is recorded at a point on the measurement grid. Secondly, the measurement is repeated over a total number of 30 spark discharges and taken average on to reduce the statistical uncertainties. The resulting standard deviation at a measurement point is less than 5% of its mean value at for all the experimental results presented in this study. Lastly, the above procedure is performed repeatedly on all the measurement points. An illustration of the experimental contour is provided in the bottom-right of Fig. 2, which depicts a snapshot when the upper half of the spherical kernel enters the measurement grid. The L-contour contains critical information to infer the kernel's size, trajectory, and thermal energy rise [33]. Therefore, the L-contour is applied in this study as the key property to evaluate the performances of different spark discharge simulation strategies. The numerical version of the L-contour is obtained by post-processing the simulation data, which is explained later in Section IV.B.

III. Modeling Strategy

As introduced in Sec. I, there have been modeling strategies proposed featuring different complexities to model the spark igniter discharge, which varies from being as sophisticated as directly solving both the electric circuit and plasma fluid [11] to be as simple as a pure energy deposition [42]. In this study, the modeling principle is to focus on capturing the pulsing effect of the kernel (e.g., reproducing the size, shape, and trajectory of the kernel), and the proposed numerical capabilities are expected to be able to either directly incorporated into an aircraft engine forced ignition simulation or to inform a proper strategy to represent the spark discharge in such a simulation. Therefore, the modeling strategies here are first adopted/proposed to be as comprehensive and accurate as possible in terms of physics-capturing, until the modeling strategies are no longer readily compatible with the existing popular turbulent combustion modelings approaches, e.g., the LES-based finite-rate chemistry approach. Then, model components that

can be safely considered as secondary by a priori experience or previous studies, e.g., buoyancy and electromagnetic forces [9, 10], are neglected. Eventually, four major modeling components are considered: a) the modeling of the electric spark discharge; b) the thermodynamic model; c) the modeling of dissociation and ionization; d) the modeling of wall and radiative heat loss, each of which is explained in the following subsections.

A. Modeling of electric spark discharge

Physically, the process of an electric spark discharge consists of three phases - the breakdown phase, the arc phase, and the glow phase [6, 43], each featuring a different time scale and energy conversion efficiency. In general, the breakdown phase is extremely fast (1 - 100 ns) and involves the most sophisticated physics, where there are existing strategies that separately address the topics of avalanche and streamers formation [44] and the non-equilibrium plasma reactions [45], which falls into a different area of study from conventional numerical combustion. In combustion-related studies, the electric breakdown phase is often drastically simplified [14, 18, 46] to an infinitely fast process assuming the mixture has relaxed to equilibrium [7]. The glow phase is the period where the electric spark is visible, has a relatively long time scale (0.1 - 10 ms), and has often been modeled as a finite-rate process coupled with the flow field evolution [11, 15]. The arc phase, which transits in between the breakdown phase and the glow phase, has a relatively short time scale $(1 - 100 \mu \text{s})$ and has been modeled either as an infinitely fast process along with the breakdown phase [15] or as a finite-rate process along with the glow phase [11].

In this study, the electric spark is modelled by the fixed-line energy deposition model implemented in CONVERGE CFD software [47]. In specific, a line-shaped energy source marked by a series of virtual particles is used to represent the electric arc, which essentially replaces any breakdown mechanism model by directly imposing a presumed electric arc channel. The spark electrical energy is then deposited into the gas phase at a prescribed power via the CFD control volumes that the line-shaped energy source overlaps with [17]. The exact formulation of the volumetric spark energy source term is shown by Eq. 2.

$$\dot{Q}_{spk} = \frac{1}{V_{cell}} \frac{n}{N} \frac{E_{spk}}{t_{spk}},\tag{2}$$

where \dot{Q}_{spk} is the volumetric energy source term, V_{cell} is the CFD cell volume, n is the number of virtual particles that a specific control volume contains, N is the total number of virtual particles applied to represent the line-shaped energy source, E_{spk} is the spark nominal energy (1.24 J) and t_{spk} is the spark discharge duration (40 μ s). To clarify, while the strategy of deposing energy has been previously applied, the difference is that, unlike many previous studies [13, 48] that calibrate the energy profile against the measured kernel *thermal energy*, here, the prescribed power profile is set exactly to the spark discharge *electric energy* [49]. Namely, the heat loss effects here are simulated instead of presumed. It should also be noted that there are other physically more accurate models [11, 12] that include the two-way interactions between the electric system and the plasma flow field, but such strategies are rarely applied in practical forced ignition

problems [15] and not considered here either.

Regarding the initiation of the electric arc channel, the fundamental mechanisms [7, 50] is sensitive to a convoluted series of factors under realistic effects. For instance, for the target configuration (Sec. II), ideally, the electrodes are flat-shaped and the gas gap should exhibit homogeneous electric impedance among all azimuthal orientations. However, any imperfection in the geometry, which is constantly evolving due to electrodes melting after each spark, could potentially alter the solid surface electric potential distribution and drastically change the next electric avalanche. Also, the gas mixture properties within the igniter cavity are subject to shot-to-shot interactions, which leads to in-homogeneous electric impedance. Therefore, little is known for the shape and position of the electric arc resulting from the initial electric breakdown, and the initialization can only be treated statistically. To handle this challenge, first, the line-shaped energy source representing the electric arc is constrained inside a plane that goes through the symmetrical axis of the igniter cavity (see Fig. 13). A parameter study is carried out in Sec. V.B to discuss how the in-plane variation of electric arc shape affects the kernel evolution. Then, a post-processing strategy is applied to reconstruct the numerical version of the *ensemble* kernel pulsing, as the statistical average of the stochastic initialization of the source plane in different azimuthal orientations (details explained in Sec. IV.B). A corresponding parameter study is carried out in (Part B, Supplemental Material) to discuss how the applied statistical distribution of the electric arc azimuthal position affects the resulting ensemble kernel behavior.

To keep the modeling setups concise, the elongation effects of the electric arc, which is expected to be small due to the short discharge time scale, are neglected and all virtual particles presenting the energy source are held stationary during the simulations. The spark discharge energy profile is available from a prior experimental study [49], which is roughly a constant power discharge that deposits a total amount of 1.24 J of energy in 40 μ s by the end of the glow phase (see blue dash line in Fig. 3).

B. Modeling of high-temperature thermodynamic

The gas thermodynamics modeling has a direct impact on the resulting kernel temperature along with other thermodynamic properties [7] that potentially affect the kernel pulsing. In most previous studies, either a comprehensive statistical thermodynamic modeling with local thermal equilibrium assumption is used [7, 9], which applies the partition function to quantify different modes of the internal energy based on kinetic theories and is valid up to very high temperature. Or, a polynomial fitting of thermodynamic properties as a function of temperature [8, 12] is applied. Theoretically, since both methods assume local thermal equilibrium, the accuracy of both methods should be comparable. Note that, based on prior studies [7, 51] and conservative evaluation, the time-scales associated with the thermal non-equilibrium processes are extremely short compared to the simulation time scale. For instance, all non-equilibrium effects should relax shortly after the drop-off of the initial voltage spike [7], which is about 100 ns for the target igniter [49]. Technically, polynomial fitting is preferred here as it is readily compatible with the commercial CFD

software used in this study. However, the fitting data is limited to a certain temperature range that is often insufficiently high to cover the hot kernel (~ 60000 K [43]). In other words, when inversely calculating the temperature based on the local energy, the resulting temperature will breach the upper limit of the polynomial fitting. The simplest method to address such energy overflow is to clip off the local energy source (i.e., the electric spark model in Sec. III.A) when the resulting temperature is about to breach the upper polynomial limit, which is implemented as the default approach in the commercial CFD software used here [47]. In a preliminary study [2], however, this method is found to lead to a kernel size much smaller than experimental observation, mainly because the energy overflow is too prominent for the high-energy aircraft igniter and leads to a major portion of the energy being clipped off. An alternative strategy, referred to here as the "energy soft clipping" method is considered, which clips not the energy source but instead the temperature and temperature-dependent thermodynamic/transport properties [34]. Compared to the first method, the energy soft clipping is more physical in terms of conserving the spark energy. The only modeling aspect that should not be given undue credence for this method is predicting the initial compression effect of the gas phase near the electric arc as well as the following gas expansion, which are demonstrated in Fig. 3 and is further discussed below.

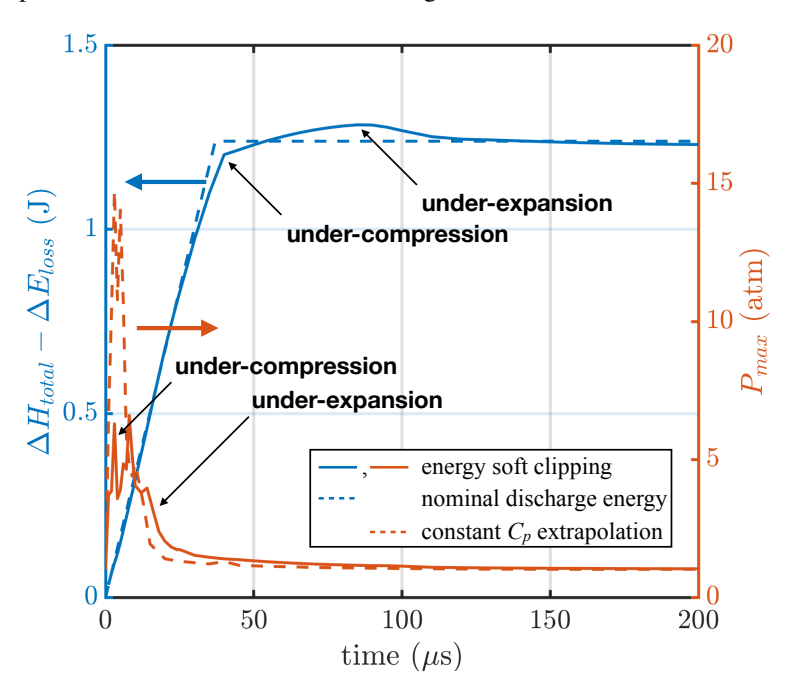


Fig. 3 Demonstration of under-compression/expansion using time histories of (left vertical axis) domain-integrated total energy rise and (right vertical axis) domain-maximum pressure obtained with different thermodynamic models.

For a compressible flow solver, a clipped pressure field will not fully adapt to the local density and temperature during the initial compression stage, where the gas evolution near the electric arc is approximately a constant volume energy deposition process [7]. For instance, the maximum pressure history predicted with the energy soft clipping (red solid line in Fig. 3) exhibits a lower spike than that with an "ideal" thermodynamic model (red dash line in Fig 3)

at the very beginning stage of the discharge, with "ideal" meaning pressure not being clipped off (further discussed later). This effect is here referred to as "under-compression", which further leads to a delay in the velocity and density field evolution and eventually in the later expansion process, here referred to as "under-expansion". In the applied compressible flow solver, only the total internal energy U (i.e., the sum of formation + sensible + kinetic energy) is transported and explicitly conserved, whereas the total enthalpy H, obtained via post-processing (i.e., H = U + PV), is exposed to the under-compression/expansion just as the pressure field. This feature leads to a metric that can be defined to quantify the overall level of the under-compression/expression, as the error between the total enthalpy rise that the CFD simulation being exposed to (blue solid line in Fig. 3) against the nominal spark energy profile (blue dash line in Fig. 3). It can be observed from Fig. 3 that this error is only a small fraction of the total enthalpy rise of the system and only lasts for a relatively short period near the end of the discharge. This is because the energy soft-clipping should be effective only temporarily and limited to locations around the electric arc, whereas shortly after the discharge the local energy overflow should dissipate out. Based on these above findings, it can be argued that the energy soft clipping provides a handy and mostly accurate resolution to the energy overflow issue. The method is therefore applied in the main simulations of this study, along with the thermodynamic polynomial coefficients obtained from the NASA CEA database [52] that are validated up to 20000 K for the species of interest.

Lastly, it is clarified that, in Fig. 3, the ideal thermodynamic result (red dash line) is obtained by extrapolating the thermodynamic polynomials at the upper limit assuming a constant heat capacity C_p [15], which is not necessarily a better modeling strategy but simply a demonstration of the concepts of under-compression/expansion. Physically, the maximum kernel temperature does not always increase with the spark energy but instead reaches a limited value, compensated by the increase of the width of the post-breakdown electric arc [6, 43]. In this case, extrapolation is not necessarily more accurate than clipping and not applied in this study. A more rigorous method is to track different modes of the internal energy by kinetic theory [53]. However, this method require further customization of the CFD software and will be pursued in the future.

C. Modeling of chemical reactions

While the igniter is mounted in a pure air environment with the presence of no fuel in this study, a chemical reaction model is still considered here as air is subject to dissociation and ionization reactions, where the reaction heat absorption/release may considerably affect the thermal expansion and kernel pulsing. To understand the basic physics and determine a proper modeling option, a preliminary study using a series of 0-d perfectly stirred reactor (PSR) calculations are performed and presented below. The chemical mechanisms applied here can be obtained from Ref.[54, 55] and the PSR calculation presented in this section is carried out using the open-source chemical kinetics suite Cantera [56].

Firstly, the significance of dissociation and ionization are studied, by performing the PSR calculation at a constant

volume with an external energy source representing the spark discharge, and are compared between finite-rate chemistry modeling of inert air (N_2 and O_2), dissociation (air + free radials: N_2 , O_2 , N, O, and NO), and plasma (air + free radicals + ions: N_2 , O_2 , N, O, NO, N_2^+ , O_2^+ , N^+ , O^+ , NO^+ , and e^-). The chemical mechanism proposed by Schulz *et al.* [54] is applied, which was originally proposed for simulating hypersonic applications but later adapted by multiple studies to model the spark discharge [38, 49]. The results are shown in Fig. 4. Note that since the 0-d calculation does not the transport effect, the PSR volume has been manually relaxed from the volume of the electric arc channel (channel width in a CFD simulation equals the minimum grid resolution) to the volume of the entire igniter cavity (4×10^{-8} m³), otherwise the energy overflow will persist throughout the PSR simulation and represent little physics. From the left of

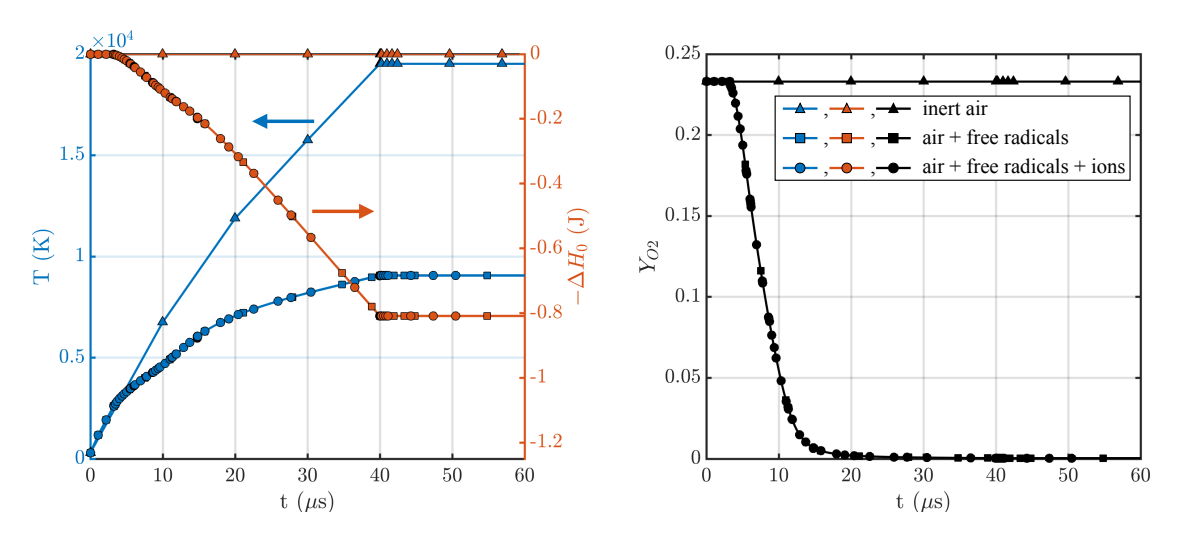


Fig. 4 Time histories of (l.h.s. plot, left vertical axis) temperature and (l.h.s. plot, right vertical axis) chemical heat absorption and (r.h.s. plot) O2 mass fraction obtained from PSR energy deposition using different chemical mechanisms.

Fig. 4, it can be found that temperature increment is significantly lowered from inert air (triangle) when dissociation (rectangle) is included, whereas further including ionization (circle) does not considerably affect the heat absorption and temperature. The right of Fig. 4 indicates that major species of O_2 has been almost depleted due to dissociation, whereas further including ionization does not significantly affect the time history of such species. It is further found that the formed ion species (right of Fig. 5) are orders of magnitudes less than their neutral species counterpart (left of Fig. 5), and therefore not insignificantly affect the formation energy and temperature. The results shown in Fig. 5 are consistent with previous studies [6, 7]. Sher *et al* [7] found that the ion relaxation after the spark breakdown phase is relatively short of $< 0.1 \ \mu s$. After the breakdown phase, the voltage drops considerably and the mechanism of ion formation becomes thermal ionization, which is negligible compared to the ionization by electrochemistry during the breakdown. Consequently, only a small fraction of gas of < 0.01% is ionized after the breakdown phase, according to Maly and Vogel [6]. Namely, ionization is only significant during the electric breakdown. Since the applied modeling of spark discharge (as well as the equivalent PSR calculation) skips the modeling of the breakdown phase, the simulation

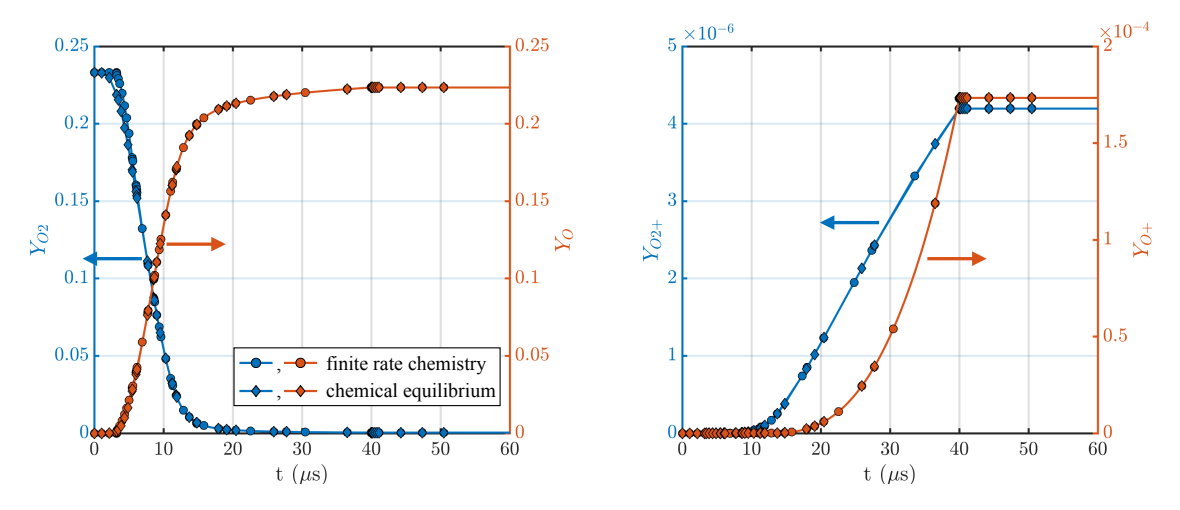


Fig. 5 Time histories of (l.h.s. plot) ground species and (r.h.s. plot) ion species mass fractions obtained from PSR calculation energy deposition using the "air + free radical + ions" version of the mechanism proposed by Schulz *et al.* [54].

results showing including ionization does not affect temperature is reasonable. From Fig. 5 it can also be seen that at the initial compression stage of the spark discharge, due to the high temperature and therefore reaction rate, the finite-rate chemistry (circle) yields almost identical results to chemical equilibrium calculation (diamond). Based on the above results, only the free radical reactions are included in the chemistry modeling in the remaining study whereas ion reactions are neglected.

Secondly, the applicability of the GRI mechanism [55] as an alternative model of the mechanism by Schulz *et al.* [54] is evaluated. In this case, all the air dissociation and NOx Zeldovich reactions within the GRI mechanism are considered (involves the species of O_2 , N_2 , NO, N, and O). Ionization effects are neglected, as above-mentioned. The reason for considering the GRI mechanism are two folds: a) during PSR calculations and preliminary 3-d CFD simulations, it is found that the mechanism of Schulz *et al.* is relatively stiff and sometimes leads to numerical instability; b) as stated at the beginning of this section, the numerical capabilities developed in this study should be readily compatible with conventional combustion simulations - it is preferred from a model compatibility aspect that the rate coefficients of air dissociation in a popular combustion mechanism are directly applicable here. For the initial energy deposition after the electric breakdown, the finite-rate chemistry results have already been shown in Fig. 5 to be very close to chemical equilibrium results. This trend still holds well for the GRI mechanism (results not shown). The remaining question is to evaluate the GRI mechanism in the later gas expansion process, which is studied using another PSR calculation of gas expansion. The PSR gas expansion is prescribed with a volume growth rate of $\dot{V} \propto (p - p_0)$ and is initialized from the end state of the PSR energy deposition in Fig. 4 and Fig. 5. No extra energy source is used. The results are shown in Fig. 6. During the PSR expansion, the GRI mechanism predicts faster recombination than the mechanism of Schulz *et al.* does. However, the difference in the delay time between the two results (about 1 μ s) is much smaller than the residence

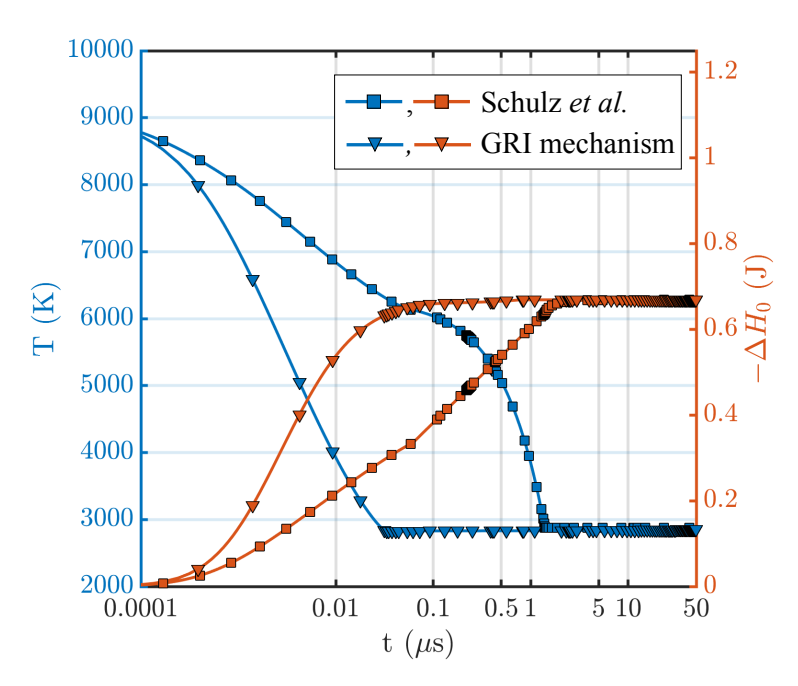


Fig. 6 Time histories of (left vertical axis) temperature and (right vertical axis) heat release obtained from PSR gas expansion using different chemical mechanisms.

time of the pulsing kernel (about 200 μ s, based on the igniter cavity diameter and the speed of sound). Therefore, the reaction rates obtained with the GRI mechanism are considered applicable and used in the main CFD simulations.

D. Modeling of heat loss

Heat loss is an important physics in the spark igniter discharge that leads to considerable differences between the nominal spark energy and the energy transmitted to the gas phase [6, 9]. For ICE engine spark plug, the conductive heat loss to the electrodes is the main mechanism of heat loss [9] that critically affects the ignition process [57]. Previous high-fidelity numerical simulations of ICE engine spark plug [9] applied either Dirichlet boundary condition of the cold wall [9] or adiabatic wall boundary to simulate the spark discharge [11]. In this study, a parameter study is performed to test both cases (Sec. V.A).

Apart from conductive heat loss, radiative heat loss has been considered by previous simulations [9–11], often, using the optically thin assumption. As the optical thickness of the target configuration is much smaller than unity (specifically, absorption coefficient times domain length scale is here less than 0.02), this assumption safely holds and is applied in this study. The optically thin radiation model proposed by Grosshandler [58] is formulated as a radiative energy sink term of

$$\dot{Q}_{rad} = 4a_p (T^4 - T_b^4),\tag{3}$$

which is a function of the local temperature T. In Eq. 3, T_b is the background temperature that is here set to room temperature; a_D is the absorption coefficient, which is modeled as a function of the temperature of a single lumped

mixture that represents the high-temperature plasma air and is integraed over the radiation wavelength, i.e., applying the grey gas approximation, as shown in Fig. 7.

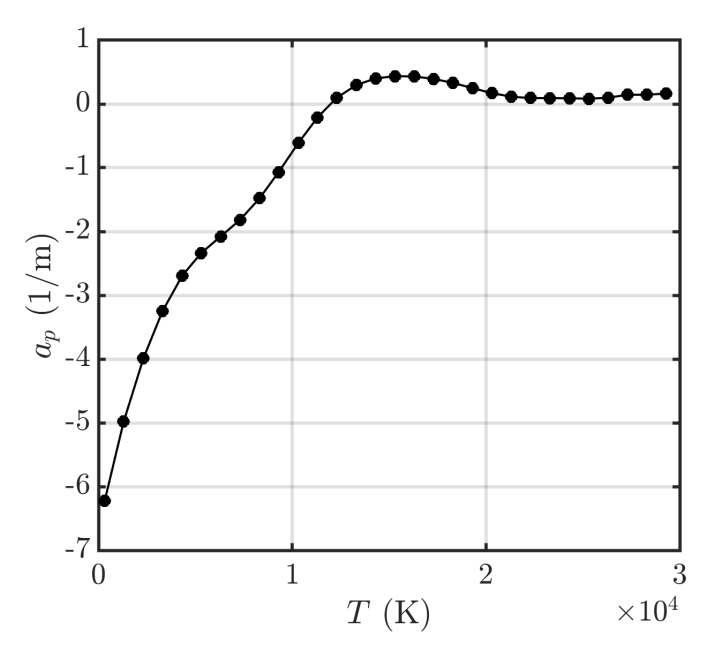


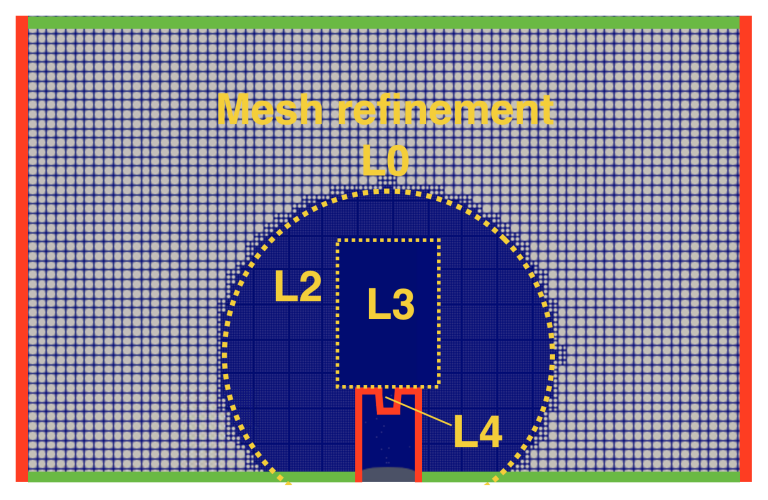
Fig. 7 Absorption coefficient of high-temperature air plasma, reconstructed by Planck-averaging over the wavelength spectrum of [30, 4500] nm with original data obtained from Ref. [59].

IV. Numerical Setups and Post-processing

A. Compressible flow LES simulation details

The target configuration consists of a section of the experimental test tube with Neumann boundary conditions applied at both ends, as shown in Fig. 8. A fixed embedded mesh is applied, which is refined near the tip of the igniter, while no adaptive mesh refinement is applied. In particular, inside the igniter cavity, the grid is most refined to have an average size of $\Delta x = 1.25 \times 10^{-4}$ m. Preliminary simulations have been performed to determine the sufficient domain scale and grid resolution prior to the main simulations, so that further refinement or enlarging the domain does not significantly impact the results. Estimated with the M criterion [60], the simulation on the final mesh resolves 95% of the turbulent kinetic energy, in terms of domain-integrated average, and 80%, in terms of domain minimum. The complete grid convergence study has been provided in Part A of the Supplemental Material. At all solid walls, a non-slip velocity boundary condition is applied for momentum, whereas either a Dirichlet boundary condition of room temperature or a Neumann boundary condition is applied for energy, which will be specified later for different test cases. All test cases are initialized from a quiescent flow at atmospheric conditions. The flow motion is spontaneously driven by the thermal expansion induced by the spark discharge, where the modelings have been explained in Sec. III.

A density-based compressible solver implemented in the commercial CFD platform CONVERGE [47] is used. The



wall boundaries (red lines): T = 300K, nonslip outflow boundaries (green lines): Neumann

Fig. 8 Schematic of the simulation domain. L labels the different mesh refinement regions with L4 being the finest level ($\Delta x = 1.25 \times 10^{-4}$ m). The boundary of L3 overlaps with the X-ray measurement window.

transport equations for mass, momentum, species, and total internal energy are solved in the LES framework. The mass transport equation is written as

$$\frac{\partial \overline{\rho}}{\partial t} + \frac{\partial (\overline{\rho} \widetilde{u_j})}{\partial x_j} = 0, \tag{4}$$

and the momentum transport equation is written as

$$\frac{\partial(\overline{\rho}\widetilde{u_i})}{\partial t} + \frac{\partial(\overline{\rho}\widetilde{u_i}\widetilde{u_j})}{\partial x_j} = -\frac{\partial\overline{P}}{\partial x_i} + \frac{\partial\overline{\sigma_{ij}}}{\partial x_j} - \frac{\partial\tau_{ij}}{\partial x_j}.$$
 (5)

In those equations, $\overline{(.)}$ and $\widetilde{(.)}$ are respectively the Reynolds-average and Favre-average operator, u is velocity, ρ is density, and P is pressure. The viscous stress tensor σ in Eq. 5 is further formulated as

$$\overline{\sigma_{ij}} = \widetilde{\mu} \left(\frac{\partial \widetilde{u_i}}{\partial x_j} + \frac{\partial \widetilde{u_j}}{\partial x_i} \right) - \frac{2}{3} \widetilde{\mu} \left(\frac{\partial \widetilde{u_k}}{\partial x_k} \delta_{ij} \right), \tag{6}$$

with μ being viscosity and δ being the Kronecker delta. The sub-grid stress tensor τ in Eq. 5 is further formulated as

$$\tau_{ij} = \overline{\rho}(\widetilde{u_i u_j} - \widetilde{u_i} \widetilde{u_j}), \tag{7}$$

which is closed using the dynamic Smagorinsky model [61]. The species transport equation is written as

$$\frac{\partial(\overline{\rho}\widetilde{Y_m})}{\partial t} + \frac{\partial(\overline{\rho}\widetilde{u_j}\widetilde{Y_m})}{\partial x_j} = \frac{\partial}{\partial x_j} \left(\overline{\rho}(\widetilde{D} + \widetilde{D_T}) \frac{\partial \widetilde{Y_m}}{\partial x_j} \right) + \widetilde{S_m}, \tag{8}$$

where Y_m denotes the mass fraction of species m. D and D_T are the molecular and turbulent mass diffusion coefficients, respectively, which are here simply obtained from the molecular and turbulent viscosity using a constant (turbulent) Schmidt number of 0.78. S_m is the chemical reaction source term, which is modelled by finite-rate chemistry, using a subset of the GRI mechanism as introduced in Sec. III.C. The ODE integration of the reaction source is calculated using the SAGE detailed chemical kinetics solver [62]. The energy transport equation is written as

$$\frac{\partial(\overline{\rho}\widetilde{E})}{\partial t} + \frac{\partial(\overline{\rho}\widetilde{E})}{\partial x_j} = -\frac{\partial(\widetilde{u_j}\overline{P})}{\partial x_j} + \frac{\partial(\widetilde{u_i}\overline{\sigma_{ij}})}{\partial x_j} + \frac{\partial}{\partial x_j}\left(\widetilde{k}\frac{\partial\widetilde{T}}{\partial x_j}\right) + \frac{\partial}{\partial x_j}\left(\overline{\rho}\widetilde{D}\sum_{m}\widetilde{h_m}\frac{\partial\widetilde{Y_m}}{\partial x_j}\right) + \dot{Q}_{spk} - \dot{Q}_{rad},\tag{9}$$

where E is the total internal energy (i.e., sensible + formation + kinetic), T is the temperature, k is the thermal conductivity, h_m denotes the enthalpy of species m, \dot{Q}_{spk} is the spark energy source in Eq. 2, and \dot{Q}_{rad} is the radiation sink in Eq. 3. The r.h.s. four terms in Eq. 9 denotes the effects of pressure work, viscous heating, heat conduction, species diffusion, and radiation, respectively. Apart from Eq. 4-9, the auxiliary equation of the ideal gas equation of state is used, along with the thermodynamic modeling in Sec. III.B, to determine the relationship between density, pressure, temperature, and internal energy. The molecular viscosity and thermal conductivity are first calculated using kinetic gas theory with the PSR calculations in Sec. III.B-III.C and then tabulated as a function of temperature to be used in the LES simulations. The pressure-velocity coupling is achieved using the PISO algorithm [63] and a compressible pressure correction equation. A second-order-accurate spatial discretization scheme [64] is used for the governing equations with a fully implicit first-order-accurate time integration scheme. The time step during the simulation was automatically determined based on the Courant-Friedrichs-Levy (CFL) numbers defined by the speed of sound, which is constrained to be lower than 1.0. The same CFD solver along with similar numerical setups has been applied to successfully simulate detonation problems in 3-d complex geometry [65], which is similar to the flow dynamics here.

The total number of cells is 3 million. It takes 1 to 4 hours of wall time to run a single simulation case using 500 cores, where the exact time depends on the number of species solved by different chemical mechanisms.

B. Post-processing of numerical ensemble gas displacement

In Sec. II, it has been explained that the X-ray diagnostics provide the ensemble results of LOS integration of density ratio (i.e., the gas displacement L). In Sec. III.A, it has been explained that the initialization of the electric arc is a chaotic process that should not be described using a deterministic set of numerical results. To handle these challenges, a specialized post-processing treatment is proposed in this section to reconstruct the numerical ensemble gas displacement, summarized by the three steps shown in Fig. 9, which is further explained below.

Step 1 shows the reconstruction of gas displacement L as the LOS integration of density ratio (Eq. 1) from a specific orientation in the azimuthal direction. The orientation of the LOS integration is quantified by the view angle α , defined as the angle between the z-axis of the local coordinate system, where the LOS is performed, and that of the global

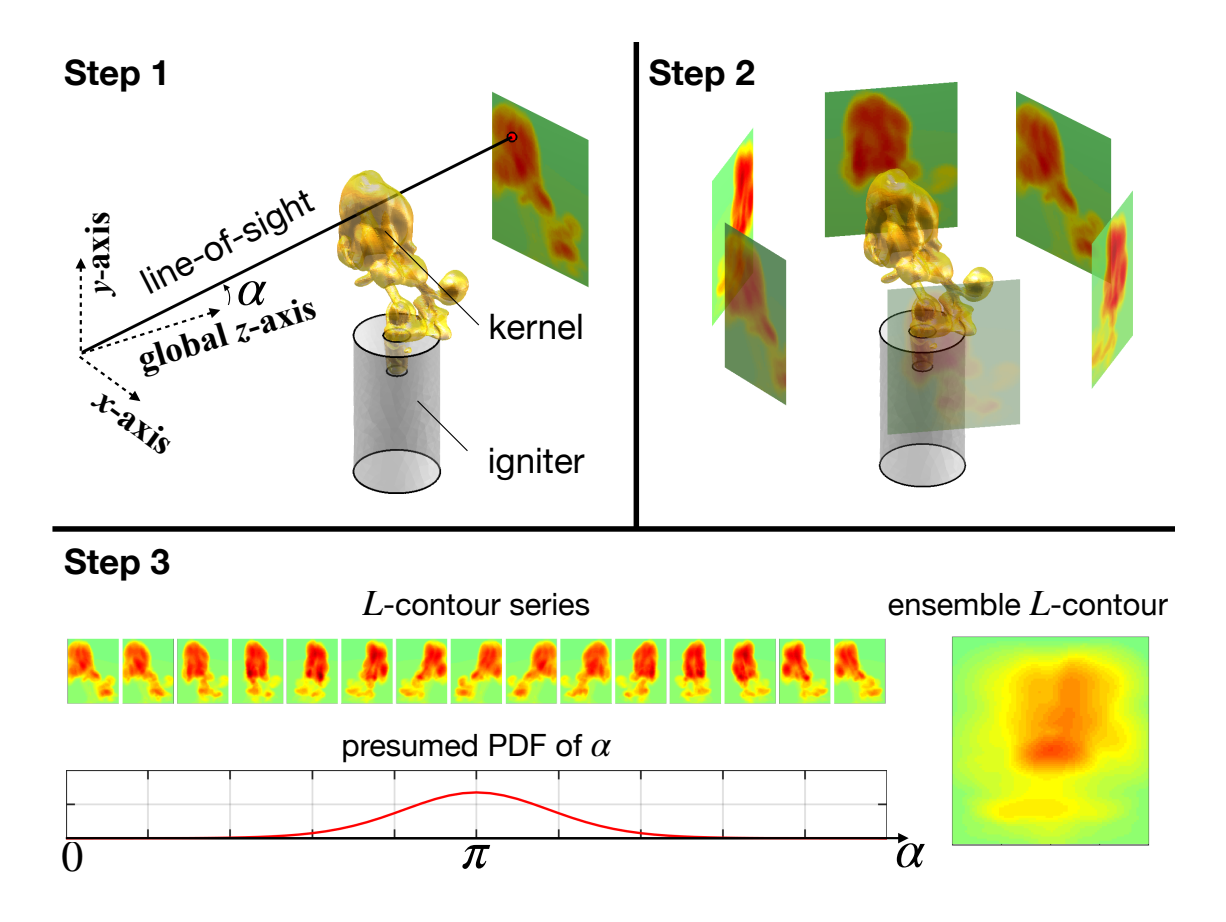


Fig. 9 Diagram of post-processing steps to obtain the numerical ensemble gas displacement. The coordinate system in Step 1 is plotted with a horizontal offset (true y-axis overlaps with the igniter central axis).

coordinate system, where the CFD simulation is performed. The output of Step 1 is a 2-d contour of gas displacement L under the local coordinates of $\{x_{\alpha}, y_{\alpha}\}$. Step 2 shows reconstructing the L-contours for a series of different view angles α and local coordinate systems. As the line-shaped energy source is not necessarily center-positioned (see Fig. 13), the resulting kernel expansion may also exhibit asymmetric patterns. Therefore, each snapshot under a different view angle may appear different (see the first row of Step 3 in Fig. 9), despite being obtained from the same set of simulation results. It is clarified that in Step 2 and Step 3 of Fig. 9, only a few snapshots of the sample series are shown, while in actual post-processing, the phase space of $\alpha = [0, 2\pi]$ is discretized using a total number of 60 snapshots at a fixed interval. Step 3 shows the reconstruction of the numerical ensemble gas displacement. The l.h.s. top row shows the sample series obtained from Step 1-2. Here, the origin of the α -axis is defined by setting the contour plane obtained under $\alpha = 0$ to overlap with the azimuthal plane in which the line-shaped energy source is constrained and meanwhile keeping the electric arc in the l.h.s. half of the plane (see Fig. 13). The l.h.s. bottom row shows the estimated distribution of the view angle weighting factor, which follows a von Mises distribution. The von Mises distribution is similar to the

Gaussian distribution but on a unit circle, and is formulated in terms of the view angle α , as

$$f_A(\alpha; \mu, \kappa) = \frac{e^{\cos(\alpha - \mu)}}{2\pi I_0(\kappa)},\tag{10}$$

with α being treated as the random variable. In Eq. 10, μ is the distribution mean, κ is a property that quantifies the distribution concentration, and I_0 can be simply taken as a normalization function. The inversion of κ is similar to the variance in a Gaussian distribution. Namely, with $\kappa \to 0$, the distribution approaches a uniform distribution, and with $\kappa \to \infty$, the distribution approaches a δ -distribution that spikes at μ . Lastly, r.h.s. of Step 3 shows the final output of the numerical ensemble gas displacement \overline{L} contour, calculated as the convolution of the snapshot series of different view angles and the presumed distribution of the weighting factor, i.e.,

$$\overline{L} = \int_0^{2\pi} L(x|_{\alpha}, y|_{\alpha}) f_A(\alpha; \mu, \kappa) d\alpha.$$
 (11)

There are several concepts to clarify to understand the above post-processing. Firstly, due to the axial-symmetry of the solid boundaries, the outputted snapshot series in Step 2 is equivalent to those obtained from a series of CFD simulations using an electric arc initialized at different azimuthal locations but sampled from a fixed view angle, without actually performing those simulations, provided any potential numerical error in those simulations does not back-propagate to affect the macroscopic flow dynamics here [26]. Secondly, for the reconstruction of the numerical ensemble gas displacement using the snapshot series, the strategy can be viewed as comparable to the X-ray diagnostics provided that the only uncertainty associated with the electric arc initialization is its azimuthal orientation. The last assumption is relatively strong while it is a handy resolution that estimates the spark discharge stochasticity using only post-processing - other strategies that rely on a weaker assumption (e.g., Monte-Carlo simulations using randomly initialized electric arc) require a further computational cost. Lastly, for the view angle weighting factor applied in Step 3, its distribution is equivalent to the statistical distribution of an electric arc forming at different azimuthal positions as if the view angle is fixed. The true value of this distribution should be affected by realistic effects (e.g. imperfections in configuration symmetry) and cannot be precisely known for this study. Without realistic effects, however, the ideal distribution should be uniform due to homogeneity and axial symmetry. In this study, the von Mises distribution is initially applied for generality and parametric study, while it is later confirmed that a uniform distribution does yield the best match against the X-ray diagnostics. Therefore, except for the corresponding parameter study (Part B, Supplemental Material), all numerical ensemble gas displacements presented in this manuscript are obtained with a uniform distribution.

V. Results and Discussions

A. Impact of wall and radiative heat loss on kernel evolution

For the first part of the discussion, the impact of heat loss (wall conduction and radiation) and absorption (dissociation reactions) modelings are studied. Figure 10 shows that the size of the pulsing kernel (hot region of the contour) becomes smaller and better matched the X-ray data with different components of heat loss/absorption is included in the simulation. Especially, comparing the Case III and Case IV of Fig. 10, the kernel size significantly reduced with radiation effect being included. While it is unsurprising that the size of the pulsing kernel should be directly related to the amount of energy converted into the gas phase sensible energy, it is informative that the modeling inclusion of different types of heat loss/absorption, particularly, radiation, is critical for the accuracy of numerical prediction here. Eventually, with all

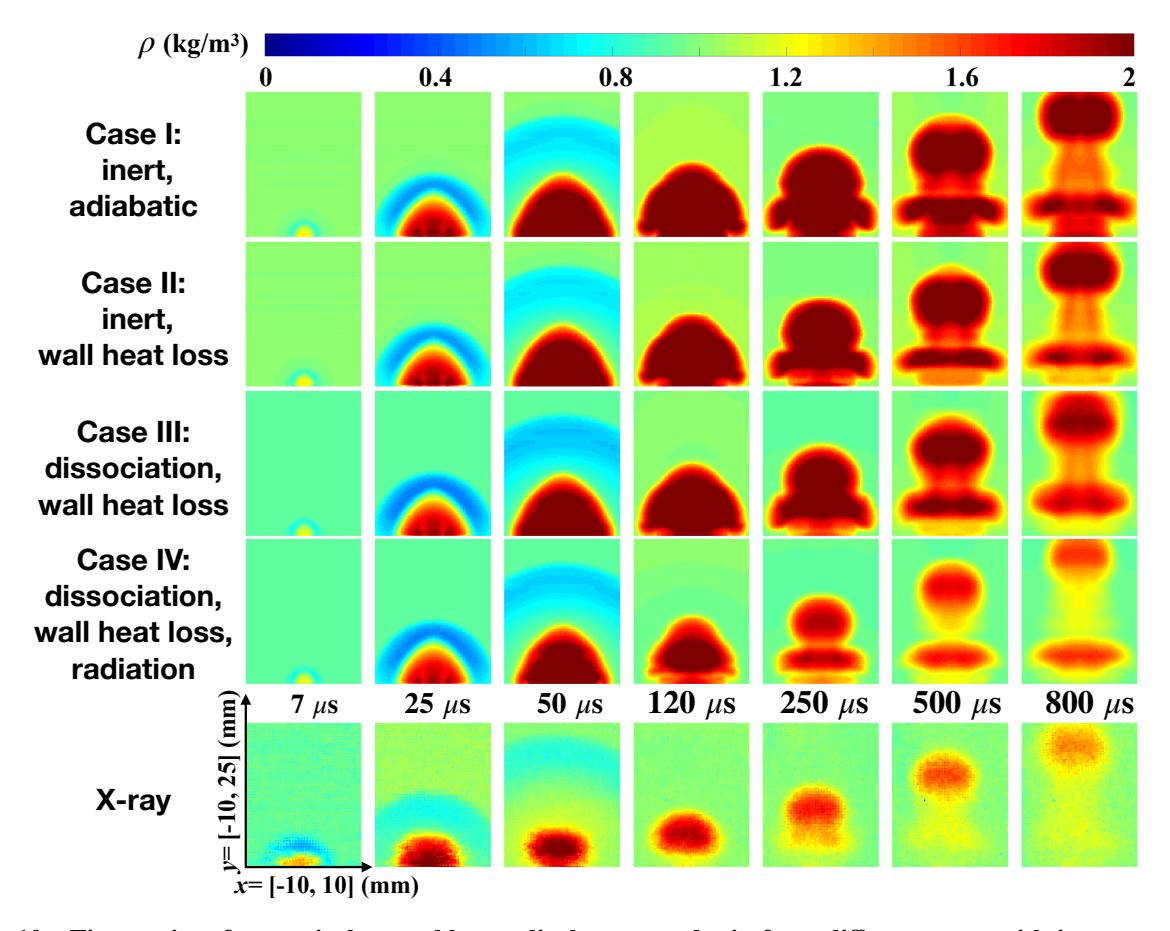


Fig. 10 Time series of numerical ensemble gas displacement obtain from different cases with incrementally included heat loss/absorption.

different types of losses/absorption included, shown by Case IV of Fig. 10, the numerical time series of ensemble gas displacement becomes qualitatively comparable against the X-ray data, except for a few issues: a) Near the bottom edge of the measurement window, the numerical simulation considerably over-predicts the gas displacement of the trailing column of the jet. Besides, the kernel size is over-predicted during $50 - 120 \mu s$. These over-predictions will

be later discussed in Sec. V.B; b) The blast wave (cold region of the contour) is overall well-captured and is barely affected by heat loss. However, the numerical results show a delay behind the X-ray time series in terms of the shock front position, which can be best visualized at 7 μ s after the electric breakdown, and a slower post-shock expansion, which can be visualized as the region behind the shock front appearing colder in the contour than the X-ray data. These two discrepancies indicate the delayed evolution of the blast wave and can be respectively explained by the under-compression and under-expansion effect as discussed in Sec. III.B.

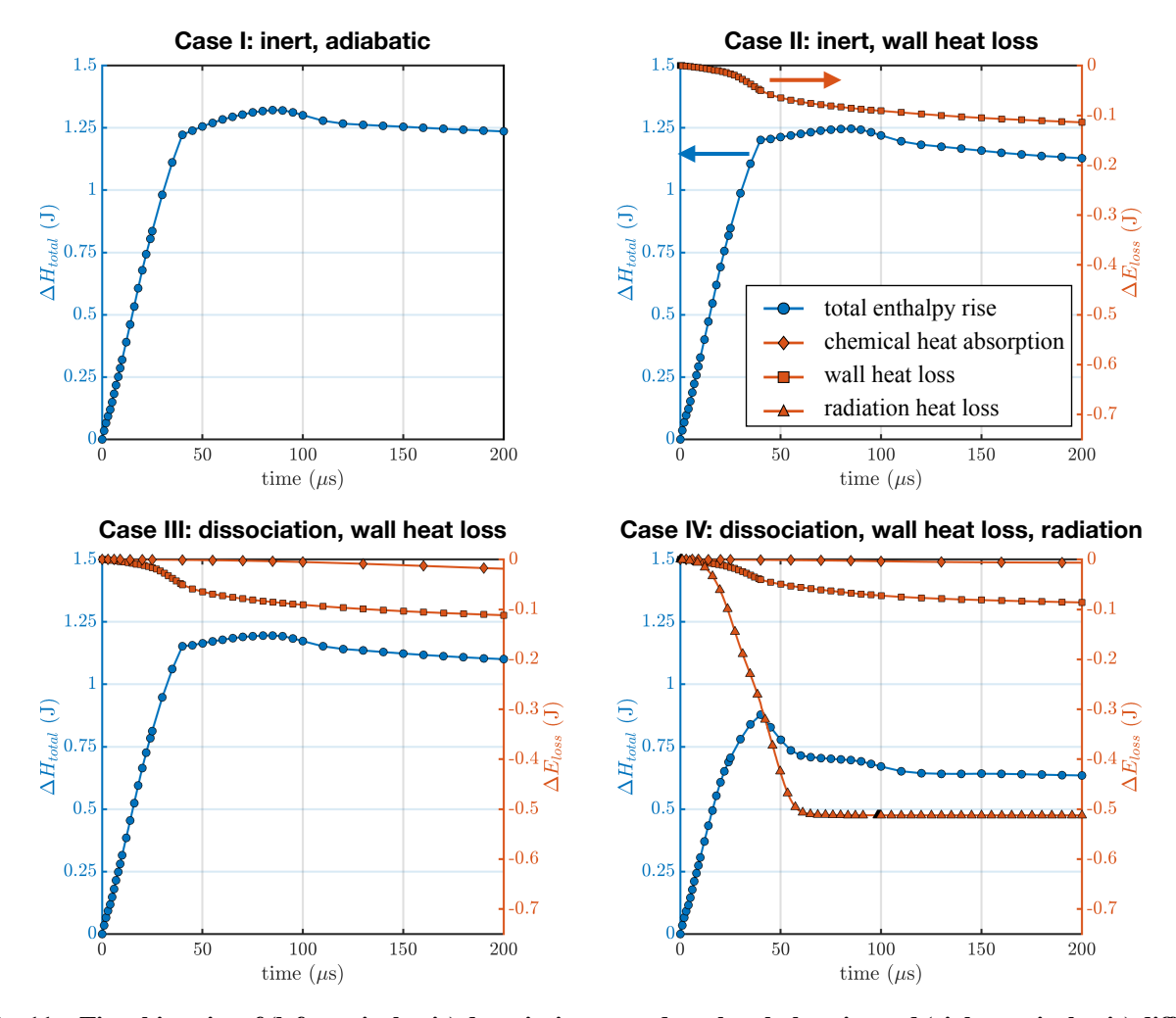


Fig. 11 Time histories of (left vertical axis) domain-integrated total enthalpy rise and (right vertical axis) different types of sensible heat losses, obtained from simulations using incrementally included heat loss/absorption.

To quantitatively investigate the energy effect, the time histories of different components of heat loss/absorption modelings and the total enthalpy rise are integrated within the simulation domain, plotted in Fig. 11. Among the three cases without radiation (Case I-III), the total enthalpy rise histories are similar for their trend, while the end value decreases from the nominal value of 1.24 J to about 1.1 J when heat loss/absorption are incrementally included. In all cases available, the radiative heat loss (about 0.5 J) contributes most of the total energy drop in enthalpy, the wall

conduction heat loss (about 0.1 J) is secondary compared to radiation, whereas the chemical heat absorption (< 0.025 J) is negligible compared to other two losses. The result is consistent with previous studies of ICE spark plugs in terms of chemical heat absorption, where the chemical potential energy initially stored in the post-breakdown plasma, after a short period of ion relaxation ($< 10 \mu s$), drops to a small fraction of the thermal energy [43]. However, the result here is different from an ICE spark plug discharge in terms of conductive and radiative heat loss, where the conductive heat loss to the electrodes was often higher than radiative heat loss [6, 9]. Such discrepancy arises from the high nominal spark energy of the aircraft igniter (Sec. I). Consequently, for the aircraft igniter, the high-temperature gas occupies a relatively large region after the electric breakdown and sustains over a long period. Note that the radiative power ($\propto T^4$), as well as the absorption coefficient (Fig. 7), grows exponentially with temperature, while the conductive heat loss power ($\propto T$), as well as the thermal conductivity [7], increases with temperature at a rate much slower than radiation does. Therefore, radiation takes over wall conduction and becomes the leading factor of heat loss in this case.

From the above contours, quantitative information of the kernel velocity and energy is extracted, as presented in Fig. 12. Here, the kernel velocity is defined by the time history of the y-position of the kernel's top edge, tracked by the steepest gradient of the gas displacement contour. The experimental kernel energy is reconstructed from the integrated kernel volume change, as

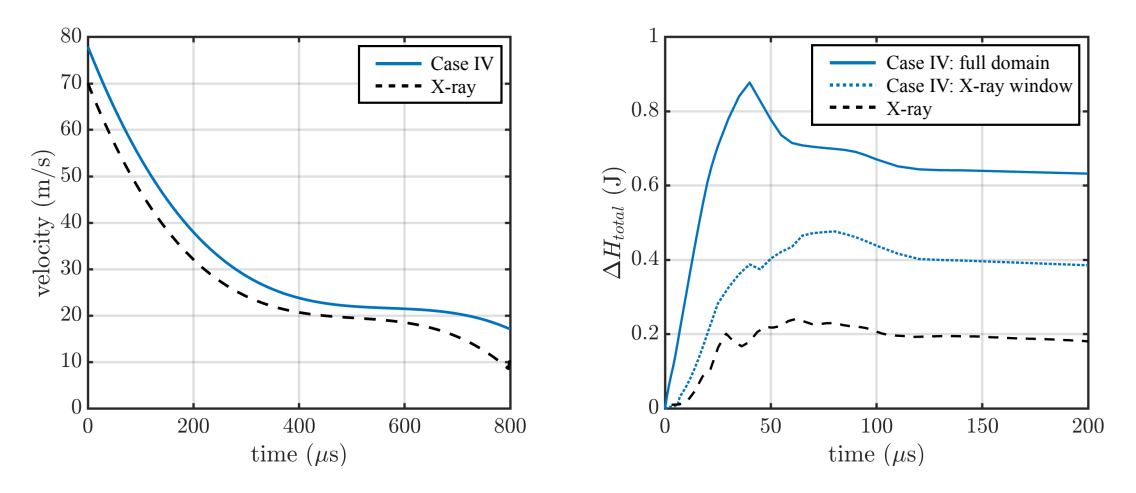


Fig. 12 Comparison of kernel velocity (left) and kernel energy (right) time histories between data obtained from Case IV and X-ray measurement.

$$\Delta H = \int \rho C_p V \, dT \approx \rho_0 C_p T_0 \iiint_V (1 - \frac{\rho}{\rho_0}) \, dV = \rho_0 C_p T_0 \iint L \, dx \, dy. \tag{12}$$

In Eq.12, the approximation is due to the assumption of a constant pressure thermal expansion process and a constant specific heat capacity, which has been applied to estimate the kernel energy of an ICE spark igniter [66]. T_0 is the ambient temperature, which is monitored to be 298.045 K in the experiment. Under such temperature, the corresponding specific heat capacity is $C_p = 1004.74$ J/kg-K. L is the X-ray gas displacement. For the numerical result, as the thermal

energy is directly accessible, the numerical kernel energy is reconstructed by integrating the total enthalpy change. As the X-ray measurement window only covers part of the domain above the igniter, for a fair comparison, the numerical kernel energy is integrated within the X-ray measurement window as well. The velocity plot in Fig. 12 shows a good match between numerical and experimental results, while the simulation slightly overestimated the kernel speed. The energy plot in Fig. 12 reveals the following new information. Firstly, although the contour plots in Fig. 10 shows qualitative match of kernel size between Case IV and the X-ray data, the quantitative comparison shows that simulation still considerably overestimated the kernel energy. This discrepancy will be later discussed in Sec. V.B. Furthermore, the numerical total enthalpy rise integrated within the X-ray measurement window (blue dash line) is found considerably lower than that integrated within the entire CFD domain (blue solid line), which suggests that the hot gas remained within the igniter cavity after the kernel ejection took up a significant amount of the gas phase thermal energy. This is an additional major mechanism of heat "loss" found for the plasma jet igniter discharge, as only the energy carried by the pulsing kernel will have an impact on the downstream ignition process.

Lastly, note that the results presented in this section are all obtained with the nominal shape of the electric arc (left of Fig. 13). While different types of heat loss can be more or less affected by the shape and position of the electric arc, which is demonstrated in the next section, the trend presented in this section holds among all shapes of electric arc tested in this study.

B. Impact of electric arc shape on kernel evolution

It has been explained in Sec. III.A that the electric arc in this study is constrained in a plane that goes through the igniter cavity axis, and the post-processing technique proposed in Sec. IV.B is applied to reproduce the stochasticity associated with the azimuthal orientation of the electric spark. The uncertainty associated with the in-plane variability of the electric arc shape, however, cannot be reproduced simply with post-processing. It is also very challenging to simulate the electric breakdown in LES, where previous effort can rarely be found. Further. Besides, due to the lack of empirical knowledge of the statistical distribution of the electric arc shape, a Monte-Carlo simulations is also inapplicable. As a compromised resolution to address this challenge, in this section, the potential impact of electric channel shape on the kernel behavior is evaluated by a parameter study. Three patterns, shown in the r.h.s. three columns of Fig. 13, are tested, chosen by intuition, to represent the situation where the electric arc shape is more convex (L-shaped) or flat (diagonal). The nominal case, shown in the first column of Fig. 13, simply applies a vertical line at the cavity center, which is nonphysical despite yielding results similar to the X-ray data (Sec. V.A) and used here as a reference result to discuss the basic physics of the kernel pulsing. Also, note that all the test cases here apply a single electric arc channel, mainly for simplicity. Theoretically, it is possible for the arc channel to branch out, known as the streamer breakdown in Ref. [50]. However, no further information is known for the configuration here as the breakdown happens within the igniter cavity that is blocked from visualization, except that a preliminary simulation using a volumetric energy

source yields a kernel size that grows considerably faster than observation, suggesting a heavily branched out electric arc channel to be unlikely.

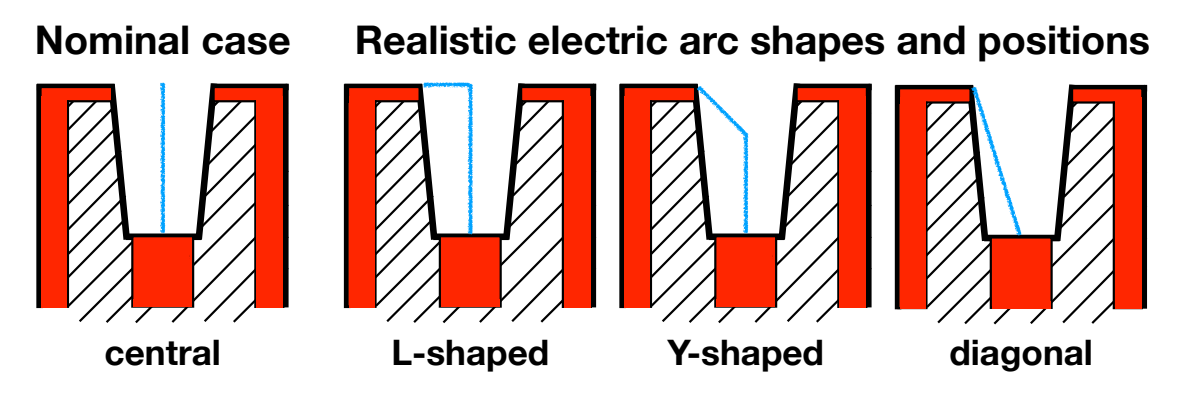


Fig. 13 Shapes of the electric arc tested in parameter study visualized at the cutting plane in which the energy sources are constrained with the electric arc (blue lines) attaching to the l.h.s. wall.

The nominal case result is presented in Fig. 14. The upper row contours of Fig. 14 show the numerical ensemble gas displacement time series, the same as the fourth row (from the top) in Fig. 10 that has already been discussed. Here, an additional observation is addressed, noticing that the spark discharge energy source is enforced for $40\mu s$, whereas the kernel expansion in the time series takes the maximum size at the snapshot at 50 µs. This means that soon after the energy source is cut off the kernel cannot sustain the thermal expansion. From the X-ray data shown in the last row of Fig. 10, similar behavior can be observed as the gas displacement contour at 50 μ s is the hottest among all snapshots. However, the initial drop of kernel size after the spark discharge (see the drop of hot contour area from the snapshots of 50 to 120 μ s) is much less prominent in the X-ray data. Since the dissipation of the kernel is positively related to its energy, this implies the kernel energy is over-predicted in the nominal case simulation at the early discharge stage, despite yielding a kernel size comparable to X-ray data at later snapshots. The bottom row contours of Fig. 14 show the density field extracted at a cutting plane through the geometry central axis. It can be observed that despite being placed at the geometry center, the kernel expansion is still slightly asymmetric, which is due to turbulence and is realization dependent - in some other simulations using slightly perturbed initial conditions, the major flow patterns are similar while the detailed flow vortex, as well as the specific direction of the kernel tilting, are different. It can also be observed from the last 4 snapshots from 120 \(\mu\)s to 800 \(\mu\)s that the region of high gas displacement near the bottom edge of the top row contours is caused by hot flow in the trailing column of the pulsing jet expanding in the radial direction. The trailing column evolves under the complex interplay between the entrainment of the cold outer flow from the kernel bottom and the remaining hot air coming out of the igniter cavity. Since the flow pattern is roughly symmetric around the central axis, so is the radial distribution in all azimuthal angles. Correspondingly, the ensemble gas displacement averaged over different view angles is relatively high in this region, which is over-predicted compared to the X-ray data shown in Fig. 10, as previously mentioned in Sec. V.A.

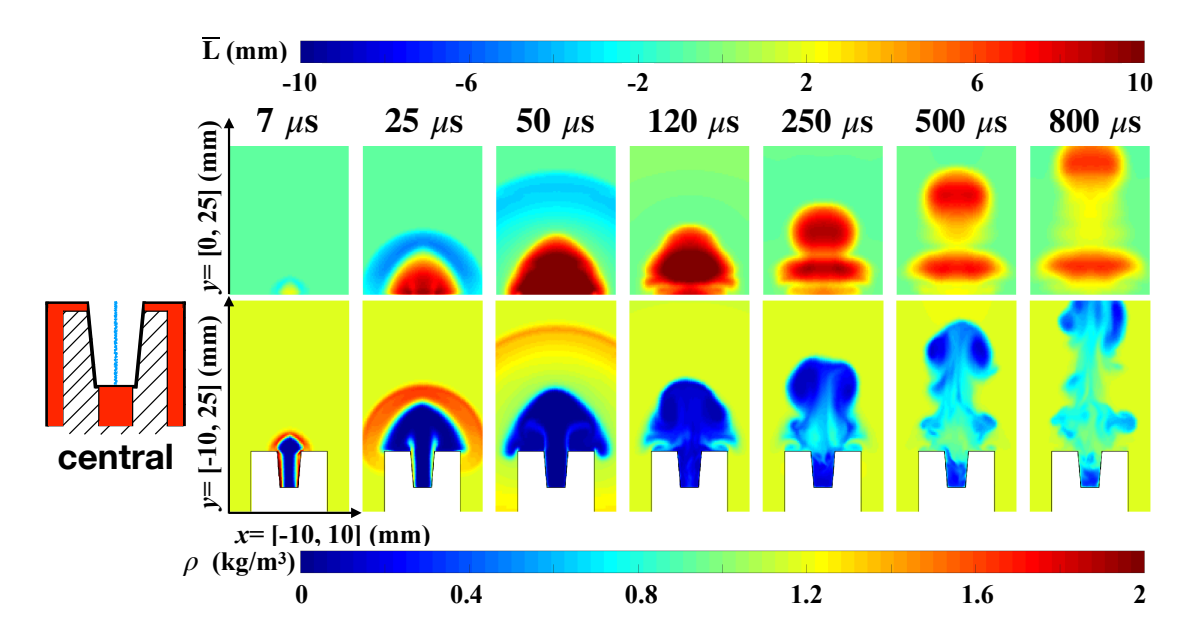


Fig. 14 Top: time series of numerical ensemble gas displacement obtained from simulations using the central electric arc. Bottom: density contour extracted at cutting planes going through geometry symmetrical axis.

The results of the three other cases are then shown in Fig. 15-17 in the same fashion as the nominal case results. Note that the cutting plane density contours are extracted at the view angle where the electric arcs attach to the solid wall on the l.h.s. of the contour (same as in Fig. 13). For the L-shaped electric arc, it can be observed from Fig. 15 that the kernel in the density contour expands faster on the l.h.s. at the early snapshots of $25 - 50\mu s$. After the spark discharge, the kernel size considerably drops on the l.h.s. during $50 - 120 \mu s$. It can also be known that, at $120 \mu s$, a vortex ring has formed, visualized as the two blobs of cold contour regions where the 3-d vortex ring intersect with the contour cutting plane. The positions of the two vortex centers exhibit asymmetry considerably more prominent than that in the nominal case, where the l.h.s. vortex center penetrates faster. The asymmetry here is no longer driven by turbulence but instead, the gas expansion from the horizontal segment of the L-shaped electric arc, which compared to the nominal case imposes an additional expansion towards the upper-right. This asymmetric expansion is best shown by the density cutting plane snapshot at 25 μ s, where the initial compression wave formed within the igniter cavity can be observed being held up to the internal sidewalls of the igniter cavity. There, the compression near the l.h.s. of the cavity wall is stronger than that on the r.h.s., as the horizontal segment of the electric arc is biased to the l.h.s. wall, providing a stronger back pressure there that eventually pushes the kernel pulsing towards the right. Due to the more off-centered distribution of kernel density, the ensemble gas displacement contour appears to be more elongated in the horizontal direction, which can be best visualized at 800 µs. For the trailing column of the pulsing jet, with the L-shaped electric arc, the asymmetric expansion causes large disruption to the flow pattern such that the radial distribution becomes larger for certain locations and smaller for the others. However, the bottom row density contours in Fig. 15 shows only part of the story, whereas from a 3-d aspect the disruption of the trailing column here is heterogeneous - the horizontal stretching

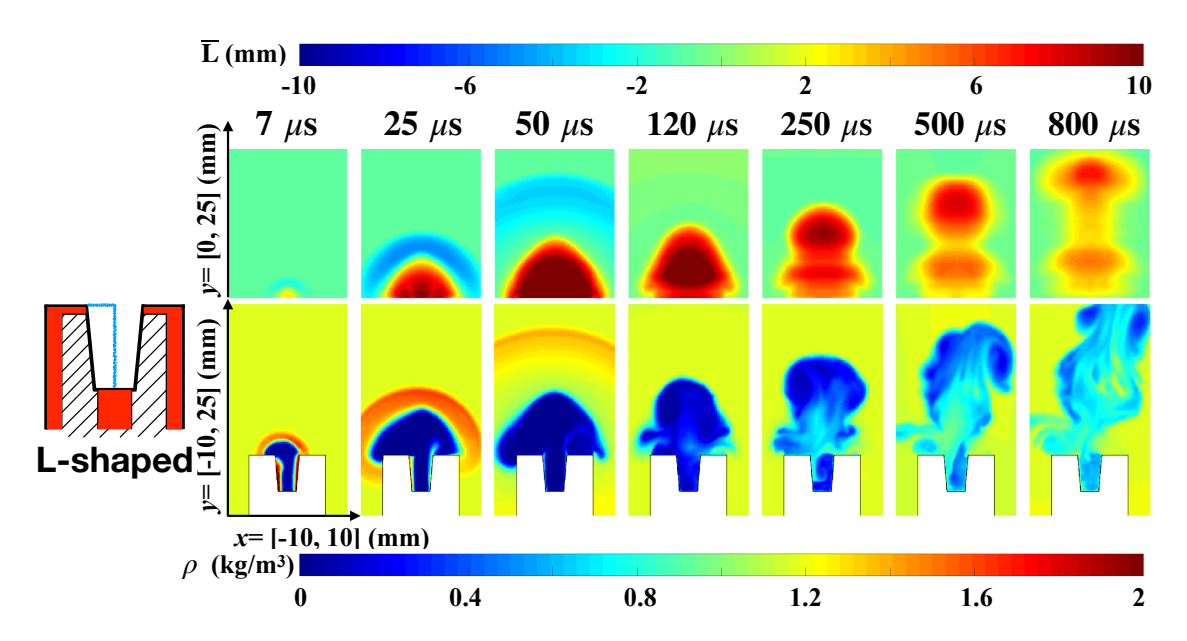


Fig. 15 Time series of gas displacement and density plotted in the same fashion as Fig. 14 but obtained from the L-shaped electric arc.

effect is stronger in the azimuthal direction of the electric arc source plane and weaker in an orthogonal direction (see the density cutting planes and gas displacement contours from different view angles in Fig. 2, Supplemental Material). This heterogeneous disruption explains the drop in the ensemble gas displacement of the jet trailing column here compared to the nominal case, as it requires a consistent density distribution under different measurement angles to achieve a high ensemble gas displacement value. It also turns out that the result here of an asymmetric trailing column is better compared to the X-ray data than the nominal case, despite still slightly over-predicting the ensemble gas displacement.

The results obtained with the Y-shaped electric arc and the diagonal electric arc are similar to those with the L-shaped channel, although observable differences do exist. Specifically, with the Y-shaped electric arc, shown in Fig. 16, the kernel tilts most off-centered among all test cases. Similar to the L-shaped electric arc case, here, the compression wave formed within the igniter cavity at the snapshot of $25 \mu s$ is stronger on the l.h.s. wall. However, in the L-shaped electric arc case, the l.h.s. compression wave facing is almost vertical, where the initial pushing effect is largely suppressed by the r.h.s. sidewall; here, due to the orientation of the upper segment of the Y-shaped electric arc, the initial compression wave formed in such region faces towards the upper-right, where the pulsing kernel is clear from the interference of the r.h.s. wall. Consequently, the kernel is directly pushed out from the cavity at an angle almost normal to the upper segment of the electric arc. Later, the kernel becomes so off-centered that the l.h.s. kernel edge completely crosses the geometry central axis in the last snapshot. Correspondingly, the ensemble gas displacement there drops significantly, similar to an asymmetric trailing jet column, as explained in the last paragraph. Compared to the X-ray data, the tilting effect here is over-predicted with the Y-shaped electric arc.

For the diagonal electric arc, the numerical results shown in Fig. 17 are overall best compared against X-ray data

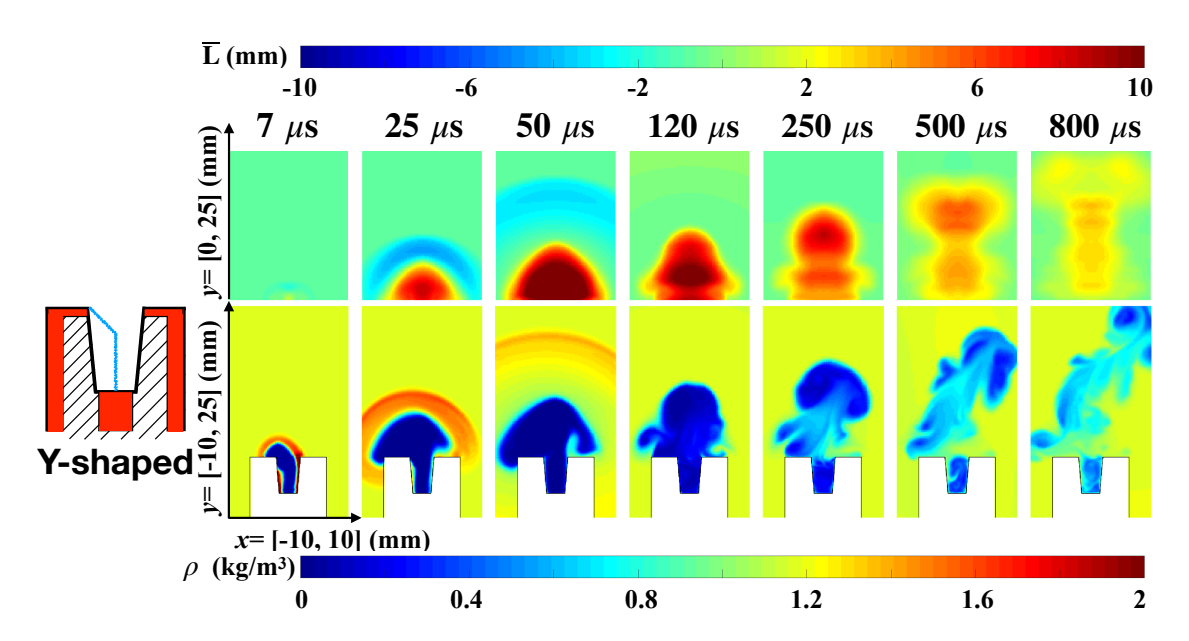


Fig. 16 Time series of gas displacement and density plotted in the same fashion as Fig. 14 but obtained from the Y-shaped electric arc.

among all cases in terms of the following aspects: a) comparing the kernel shape at later snapshots ($500 - 800\mu s$) against the X-ray data, the diagonal electric arc result is better than the L-shaped and Y-shaped results while worse than the nominal case result; b) comparing the trailing jet gas displacement at later snapshots, the diagonal electric arc result is best compared against the X-ray data among all cases; c) comparing the kernel size at early snapshots ($25 - 120 \mu s$), the diagonal electric arc result is best compared against the X-ray data among all cases. More in-depth interpretations of the results are discussed below.

Firstly, as explained for the Y-shaped electric arc, the tilting of the kernel is directly related to the orientation of the upper segment of the electric arc. Here, the effective slope of the diagonal electric arc is between the Y-shaped and the L-shaped, and the resulting kernel tilting, as well as off-centering, is between the corresponding two cases. The ensemble gas displacement of the kernel at 800 μ s is mixed compared against the X-ray data, which well-captured the gas displacement magnitude while slightly over-predicted the horizontal elongation of the kernel shape. Secondly, the trailing column of the pulsing jet in the diagonal electric arc case is further stretched horizontally in the contour plane compared to that in the Y-shaped electric arc case, suggesting more chaotic flow dynamics. This is possibly due to the asymmetric shape of the electric arc even at the lower segment of the igniter cavity that leads to complicated wave reflections and flow dynamics within the igniter cavity. For instance, the snapshots of 250 μ s and 800 μ s show cutting plane density contours that are completely the opposite around the central axis, where such bouncing is either not found or less prominent in other cases and is an indication of the complex flow dynamics here. The corresponding ensemble gas displacement of the trailing column of the pulsing jet is the lowest and best compared against X-ray data among all cases. Last, the over-prediction of kernel size at the early stage following the spark discharge stage (50 – 120 μ s) in the

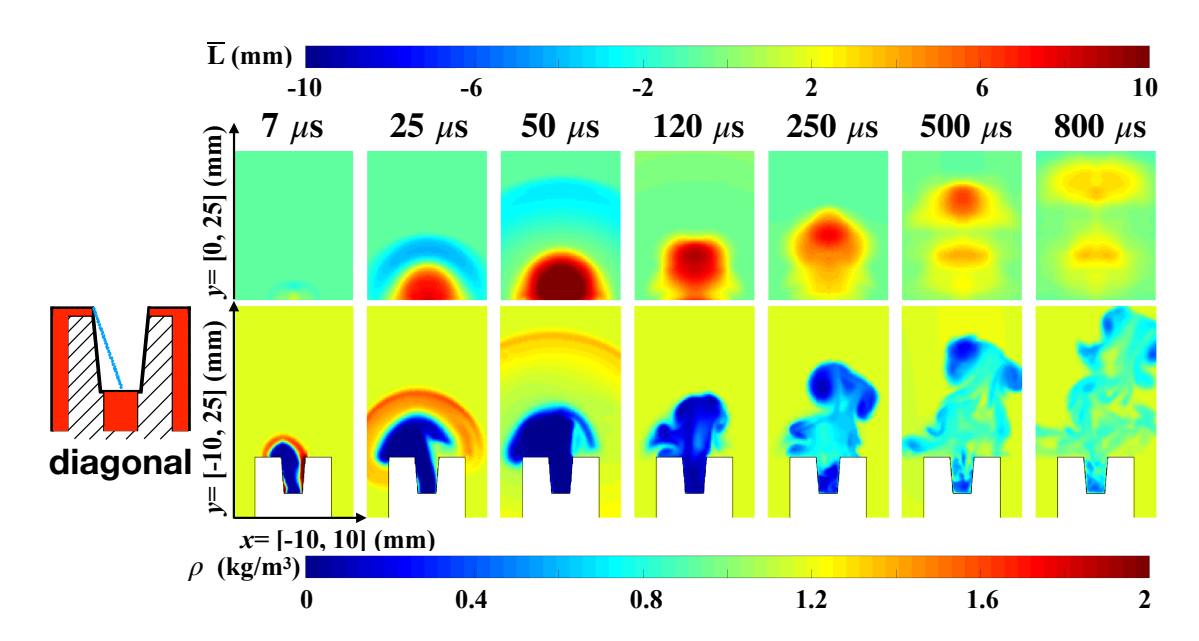


Fig. 17 Time series of gas displacement and density plotted in the same fashion as Fig. 14 but obtained from the diagonal electric arc.

nominal case and L-shaped electric arc case is also improved here. The mechanism behind this improvement is related to heat loss as discussed below.

Figure 18 shows the time histories of total enthalpy rise, total wall heat loss, and total radiative heat loss in simulations using different shapes of the electric arc. The total enthalpy rise, compared to the nominal case (solid) is

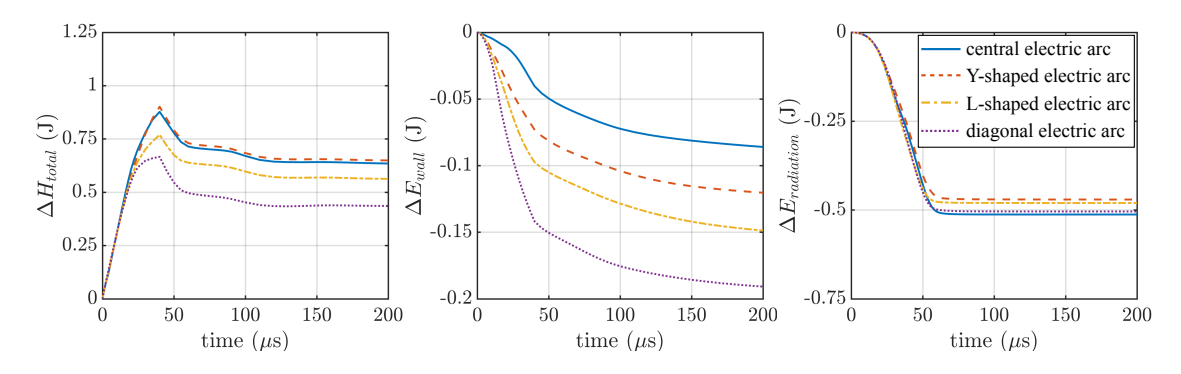


Fig. 18 Time histories of integrated (left) total enthalpy rise, (middle) radiative heat loss and (right) wall heat loss obtained from simulation cases using different electric arc shapes.

noticeably lower in the Y-shaped electric arc case (dash-dotted) and appreciably lower in the diagonal electric arc case (dotted). The drop in total energy rise is mostly due to the increment of wall heat loss in the cases of Y-shaped arc and diagonal electric arc, whereas the radiative heat loss remains roughly the same in all cases. The mechanism behind the difference in wall heat loss can be intuitively explained by the effective distance between the electric arc and the igniter cavity wall, which is the largest for the nominal case and the lowest for the diagonal electric arc case. Note that a shorter wall distance here affects the conductive heat loss not necessarily by increasing the near-wall temperature gradient, but

also by shortening the initial delay time it takes for the expanding hot gas to reach the solid wall.

A quantitative comparison between the diagonal electric arc case and the X-ray measurement is carried out, as shown in Fig. 19, using the same post-processing method to obtain Fig. 12. It can be seen that, with the same model settings, the numerical results are improved when the electric arc shape is changed from central to diagonal for both kernel velocity and kernel energy. In particular, as the wall heat loss further brings down the kernel energy, the kernel energy obtained with the diagonal electric arc is quantitatively comparable to the experimental result.

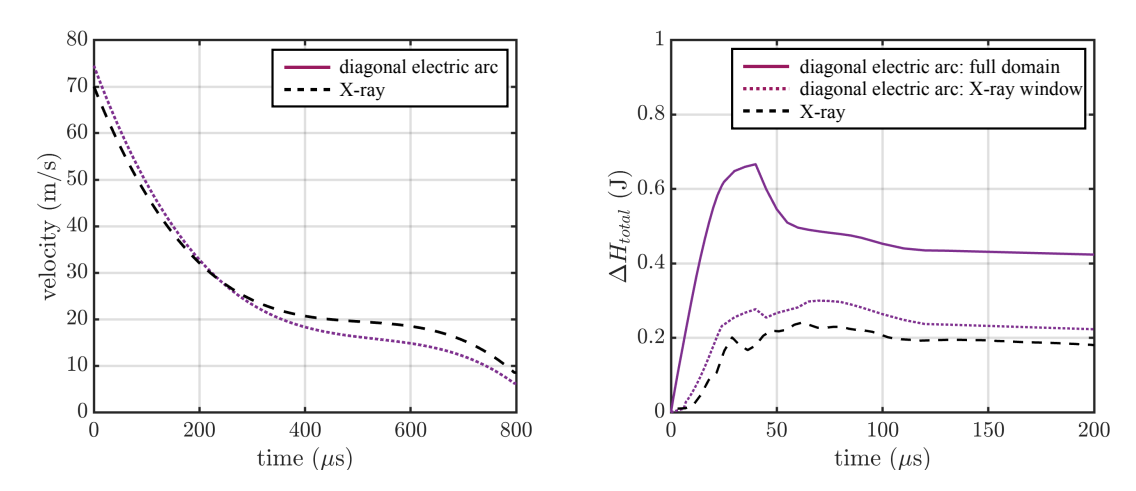


Fig. 19 Comparison of kernel velocity (left) and kernel energy (right) time histories between data obtained from diagonal electric arc case and X-ray measurement.

As a quick summary, the shape of the electric arc affects both wall heat loss as well as the pulsing of the kernel. Specifically, the electric arc effectively closer to the igniter cavity sidewall leads to a larger wall heat loss and therefore a smaller kernel size. The tilting of the pulsing kernel is directly related to the orientation of the upper segment of the electric arc. The trailing column of the pulsing jet is disrupted by the complex flow dynamics generated when the electric arc, especially the lower segment, is off-centered. Overall, numerical results obtained with the diagonal electric arc are best compared and quantitatively comparable against X-ray data.

In addition to the above analysis, statistical analysis of spark discharge on kernel behavior was conducted. This study is reported in Part B of the Supplemental Material. Based on this analysis, the spark discharge process occurs as follows: a) the electric arc yield from the initial electric breakdown is attached to the outer and central electrodes following a diagonal line of the cavity cross-section; b) the formation of the electric arc does not show any preference for particular azimuthal direction; c) the resulting kernel evolution leads to asymmetric kernel shapes and off-centered kernel penetrations in individual spark discharge sequences, while the reconstructed ensemble gas displacement shows a smooth and elliptic kernel shape.

With the results discussed in the previous sections, a summary of the contribution to energy budget is shown in Tab. 1. The energy levels are determined based on extreme values collected from simulation cases presented in Sec. V.B,

and are sampled at $t = 300 \,\mu\text{s}$, after the kernel is fully ejected out of the igniter cavity. The intention here is to emphasize mechanisms found in this study to cause the kernel energy to be significantly lower than the nominal spark energy. More specifically, radiative heat loss and residual hot gas within the discharge cavity are found to be the two major factors. Besides, wall heat loss, being sensitive to the initial shape and position of the electric arc channel, can also be important.

Table 1 A quantitative summary of energy conversions/losses of the studied plasma jet igniter discharge.

Types of energy conversion/loss	Energy	Percentage
Nominal spark energy	1.24 J	100 %
Gas dissociation heat absorption	<0.01 J	<0.8 %
Radiative heat loss	0.49-0.51 J	39.5-41.1 %
Wall heat Loss	0.085-0.21 J	6.8-16.9 %
Energy of gas remained within igniter cavity	0.24-0.25 J	19.4-20.1 %
Energy of the pulsing kernel	0.23-0.39 J	18.5-31.5 %

VI. Conclusion

In this study, the discharge process of a commercial aircraft igniter featuring the configuration of a plasma jet igniter is studied using high-fidelity numerical simulation. Due to sparsely found previous studies of aircraft spark igniters, existing modeling approaches – mostly in the ICE community, partially in the aircraft community – and fundamental knowledge generated in the spark-ignition field are reviewed in detail (Sec. I). A comprehensive set of modeling features are then adopted from existing strategies and extended to target the specific problem of this study, which includes four major components of the spark discharge process, i.e., the thermodynamic modeling, the plasma reaction modeling, and the heat loss modeling (Sec. III). A post-processing technique is proposed to estimate the ensemble kernel behavior using a single simulation run and presumed statistics of spark locations (Sec. IV.B).

Using nominal modeling setups, the numerical simulation qualitatively captures the spark discharge process in terms of the kernel shape and blast wave propagation while over-predicts the kernel size and trailing hot gas. A detailed analysis (Sec. V.A) reveals the kernel size is directly related to the loss/absorption of heat, where the leading factor is found here to be radiation instead of wall conduction, which is different from an ICE engine spark plug. Using a parameter study of electric arc shapes (Sec. V.B), the kernel tilting is found to be affected by the orientation of the upper segment of the electric arc; the trailing column of the pulsing jet is disrupted by the complex flow dynamics generated when the electric arc, particularly the lower segment, is off-centered; whereas the kernel size gets smaller when the effective distance between the electric arc and the wall is reduced. Combined with another parameter study of the presumed spark location distribution (Part B, Supplemental Material), the electric arc generated from the initial breakdown is estimated to be roughly equal-likely in all azimuthal angles and follows the shape of a diagonal line

connecting the outer and central radius. Such a modeling setup leads to an off-center kernel pulsing and asymmetric kernel shape in individual spark discharge sequence while symmetric ensemble kernel behavior that is overall best compared against X-ray data among all test cases. These results show the source of energy loss and variability in kernel strength and evolution in plasma igniters. The modeling framework used here can be integrated with combustion approaches in order to simulate the full ignition problem or used to perform a separate simulation prior to the ignition problem simulation to inform its initialization.

Acknowledgement

This presentation has been jointly created by University of Michigan and UChicago Argonne, LLC. Operator of Argonne National Laboratory ("Argonne"). Argonne, a U.S. Department of Energy Office of Science laboratory, is operated under Contract No. DE-AC02-06CH11357. The U.S. Government retain for itself, and others acting on its behalf, a paid-up nonexclusive, irrevocable worldwide license in said article to reproduce, prepare derivative works, distributed copies to the public, and perform publicly and display publicly, by or on behalf of the Government. The Argonne authors would like to acknowledge the U.S. Department of Energy (DOE), Office of Energy Efficiency and Renewable Energy (EERE), Vehicle Technologies Office (VTO), Advanced Combustion Engines Program Managers: Michael Weismiller and Gurpreet Singh. Computational work leveraged the high-performance computing capabilities at the Laboratory Computing Resource Center (LCRC) at Argonne. Experimental work presented in this paper was performed at the 7-BM beamline at the Advanced Photon Source (APS) at Argonne. This project is conducted during a visit appointment of Yihao Tang to Argonne. Yihao Tang wishes to thank Dr. Sibendu Som for the invitation. Yihao Tang also wishes to thank Dr. Junjun Guo for providing insights into radiation modeling.

References

- [1] Lefebvre, A. H., and Ballal, D. R., *Gas Turbine Combustion: Alternative Fuels and Emissions*, 3rd ed., CRC Press, Boca Raton, 2010, Chap. 5. https://doi.org/10.1201/9781420086058.
- [2] Tang, Y., "Numerical Prediction of Turbulent Non-Premixed Forced Ignition in Altitude Relight," Ph.D. thesis, University of Michigan, Ann Arbor, 2021. https://doi.org/10.7302/1454.
- [3] Ballal, D., and Lefebvre, A., "The Influence of Spark Discharge Characteristics on Minimum Ignition Energy in Flowing Gases," Combustion and Flame, Vol. 24, 1975, pp. 99–108. https://doi.org/10.1016/0010-2180(75)90132-7.
- [4] Essmann, S., Markus, D., and Maas, U., "Investigation of the Spark Channel of Electrical Discharges Near the Minimum Ignition Energy," *Plasma Physics and Technology*, Vol. 3, No. 3, 2016, pp. 116–121. https://doi.org/10.14311/ppt.2016.3.116.
- [5] Kono, M., Kumagai, S., and Sakai, T., "The Optimum Condition for Ignition of Gases by Composite Sparks," *Symposium (International) on Combustion*, Vol. 16, Elsevier, 1977, pp. 757–766. https://doi.org/10.1016/S0082-0784(77)80369-X.

- [6] Maly, R., and Vogel, M., "Initiation and Propagation of Flame Fronts in Lean CH4-Air Mixtures by the Three Modes of the Ignition Spark," *Symposium (International) on Combustion*, Vol. 17, Elsevier, 1979, pp. 821–831. https://doi.org/10.1016/S0082-0784(79)80079-X.
- [7] Sher, E., Ben-Ya'ish, J., and Kravchik, T., "On the Birth of Spark Channels," *Combustion and Flame*, Vol. 89, No. 2, 1992, pp. 186–194. https://doi.org/10.1016/0010-2180(92)90027-M.
- [8] Kono, M., Niu, K., Tsukamoto, T., and Ujiie, Y., "Mechanism of Flame Kernel Formation Produced by Short Duration Sparks," Symposium (International) on Combustion, Vol. 22, Elsevier, 1989, pp. 1643–1649. https://doi.org/10.1016/S0082-0784(89)80176-6.
- [9] Kravchik, T., Sher, E., and Heywood, J., "From Spark Ignition to Flame Initiation," *Combustion Science and Technology*, Vol. 108, No. 1-3, 1995, pp. 1–30. https://doi.org/10.1080/00102209508960387.
- [10] Reinmann, R., and Akram, M., "Temporal Investigation of a Fast Spark Discharge in Chemically Inert Gases," *Journal of Physics D: Applied Physics*, Vol. 30, No. 7, 1997, p. 1125. https://doi.org/10.1088/0022-3727/30/7/010.
- [11] Thiele, M., Selle, S., Riedel, U., Warnatz, J., and Maas, U., "Numerical Simulation of Spark Ignition Including Ionization," *Proceedings of the Combustion Institute*, Vol. 28, No. 1, 2000, pp. 1177–1185. https://doi.org/10.1016/S0082-0784(00)80328-8.
- [12] Thiele, M., Warnatz, J., Dreizler, A., Lindenmaier, S., Schießl, R., Maas, U., Grant, A., and Ewart, P., "Spark Ignited Hydrogen/Air Mixtures: Two Dimensional Detailed Modeling and Laser Based Diagnostics," *Combustion and Flame*, Vol. 128, No. 1-2, 2002, pp. 74–87. https://doi.org/10.1016/S0082-0784(00)80328-8.
- [13] Sforzo, B., Lambert, A., Kim, J., Jagoda, J., Menon, S., and Seitzman, J., "Post Discharge Evolution of a Spark Igniter Kernel," *Combustion and Flame*, Vol. 162, No. 1, 2015, pp. 181–190. https://doi.org/10.1016/j.combustflame.2014.07.024.
- [14] Fan, L., Li, G., Han, Z., and Reitz, R. D., "Modeling Fuel Preparation and Stratified Combustion in a Gasoline Direct Injection Engine," *SAE Transactions*, 1999, pp. 105–119. https://doi.org/10.4271/1999-01-0175.
- [15] Duclos, J., and Colin, O., "Arc and Kernel Tracking Ignition Model for 3D Spark-Ignition engine calculations," *The Proceedings of the International Symposium on Diagnostics and Modeling of Combustion in Internal Combustion Engines*, The Japan Society of Mechanical Engineers, Nagoya, Japan, 2001, pp. 343–350. https://doi.org/10.1299/jmsesdm.01.204.46.
- [16] Richard, S., Colin, O., Vermorel, O., Benkenida, A., Angelberger, C., and Veynante, D., "Towards Large Eddy Simulation of Combustion in Spark Ignition Engines," *Proceedings of the Combustion Institute*, Vol. 31, No. 2, 2007, pp. 3059–3066. https://doi.org/10.1016/j.proci.2006.07.086.
- [17] Scarcelli, R., Zhang, A., Wallner, T., Som, S., Huang, J., Wijeyakulasuriya, S., Mao, Y., Zhu, X., and Lee, S.-Y., "Development of a Hybrid Lagrangian–Eulerian Model to Describe Spark-Ignition Processes at Engine-Like Turbulent Flow Conditions," *Journal of Engineering for Gas Turbines and Power*, Vol. 141, No. 9, 2019. https://doi.org/10.1115/1.4043397.

- [18] Colin, O., and Truffin, K., "A Spark Ignition Model for Large Eddy Simulation based on an FSD Transport Equation (ISSIM-LES)," *Proceedings of the Combustion Institute*, Vol. 33, No. 2, 2011, pp. 3097–3104. https://doi.org/10.1016/j.proci.2010.07.023.
- [19] Wang, T., Zhang, X., Xu, J., Zheng, S., and Hou, X., "Large-Eddy Simulation of Flame-Turbulence Interaction in a Spark Ignition Engine Fueled with Methane/Hydrogen/Carbon Dioxide," *Energy Conversion and Management*, Vol. 104, 2015, pp. 147–159. https://doi.org/10.1016/j.enconman.2015.05.030.
- [20] Kim, J., Gururajan, V., Scarcelli, R., Biswas, S., and Ekoto, I., "Modeling Nanosecond-Pulsed Spark Discharge and Flame Kernel Evolution," *Journal of Energy Resources Technology*, Vol. 144, No. 2, 2022. https://doi.org/10.1115/1.4051144.
- [21] Badawy, T., Bao, X., and Xu, H., "Impact of Spark Plug Gap on Flame Kernel Propagation and Engine Performance," *Applied Energy*, Vol. 191, 2017, pp. 311–327. https://doi.org/10.1016/j.apenergy.2017.01.059.
- [22] Straub, S. W., "Surface Gap Igniter," U.S. Patent No. 5,187,404., 1993.
- [23] Clements, R., Smy, P., and Dale, J., "An Experimental Study of the Ejection Mechanism for Typical Plasma Jet Igniters," *Combustion and Flame*, Vol. 42, 1981, pp. 287–295. https://doi.org/10.1016/0010-2180(81)90163-2.
- [24] Smy, P., Clements, R., Simeoni, D., and Topham, D., "Plasma Expulsion from the Plasma Jet Igniter," *Journal of Physics D: Applied Physics*, Vol. 15, No. 11, 1982, p. 2227. https://doi.org/10.1088/0022-3727/15/11/015.
- [25] Tang, Y., Hassanaly, M., Raman, V., Sforzo, B., and Seitzman, J., "A Comprehensive Modeling Procedure for Estimating Statistical Properties of Forced Ignition," *Combustion and Flame*, Vol. 206, 2019, pp. 158–176. https://doi.org/10.1016/j. combustflame.2019.04.045.
- [26] Hassanaly, M., Tang, Y., Barwey, S., and Raman, V., "Data-Driven Analysis of Relight variability of Jet Fuels induced by Turbulence," *Combustion and Flame*, Vol. 225, 2021, pp. 453–467. https://doi.org/10.1016/j.combustflame.2020.11.025.
- [27] Mastorakos, E., "Ignition of Turbulent Non-Premixed Flames," *Progress in Energy and Combustion Science*, Vol. 35, No. 1, 2009, pp. 57–97. https://doi.org/10.1016/j.pecs.2008.07.002.
- [28] Bradley, D., and Critchley, I., "Electromagnetically Induced Motion of Spark Ignition Kernels," *Combustion and Flame*, Vol. 22, No. 2, 1974, pp. 143–152. https://doi.org/10.1016/S0010-2180(74)80001-5.
- [29] Cetegen, B., Teichman, K., Weinberg, F., and Oppenheim, A., "Performance of a Plasma Jet Igniter," *SAE Transactions*, 1980, pp. 246–259. https://doi.org/10.4271/800042.
- [30] Bane, S., Shepherd, J., Kwon, E., and Day, A., "Statistical Analysis of Electrostatic Spark Ignition of Lean H2/O2/Ar Mixtures," International Journal of Hydrogen Energy, Vol. 36, No. 3, 2011, pp. 2344–2350. https://doi.org/10.1016/j.ijhydene.2010.05.082.
- [31] Okhovat, S., "Temperature Evolution of Spark Kernels in Quiescent and Cross-Flow Conditions," Master's thesis, Oregon State University, Corvallis, 2015. URL https://ir.library.oregonstate.edu/concern/graduate_thesis_or_dissertations/dz010t373.

- [32] Cai, B., Song, H., Wu, Y., Jia, M., and Zhang, Z., "Experimental Investigation on Swirling Spray Forced Ignition of Embedded Multi-Channel Plasma Igniter," *Acta Astronautica*, Vol. 179, 2021, pp. 670–679. https://doi.org/10.1016/j.actaastro.2020.10.049.
- [33] Sforzo, B., Matusik, K., Kastengren, A., Powell, C., and Seitzman, J. M., "Aircraft Ignition Kernel Characterization by X-ray Radiography," 57th AIAA Aerospace Sciences Meeting, AIAA Paper 2019-2246, 2019. https://doi.org/10.2514/6.2019-2246.
- [34] Pillai, S. V., "Numerical Simulation of Forced Ignition LES Coupled with a Tabulated Detailed Chemistry Approach," Ph.D. thesis, INSA de Rouen, Rouen (France), 2010. URL https://tel.archives-ouvertes.fr/tel-00557901.
- [35] Boileau, M., Staffelbach, G., Cuenot, B., Poinsot, T., and Bérat, C., "LES of an Ignition Sequence in a Gas Turbine Engine," *Combustion and Flame*, Vol. 154, No. 1-2, 2008, pp. 2–22. https://doi.org/10.1016/j.combustflame.2008.02.006.
- [36] Triantafyllidis, A., Mastorakos, E., and Eggels, R., "Large Eddy Simulations of Forced Ignition of a Non-Premixed Bluff-Body Methane Flame with Conditional Moment Closure," *Combustion and Flame*, Vol. 156, No. 12, 2009, pp. 2328–2345. https://doi.org/10.1016/j.combustflame.2009.05.005.
- [37] Rieth, M., Borghesi, G., and Chen, J. H., "DNS of Post-Discharge Plasma Ignition Evolution Relevant to High Altitude Relight."
 Tech. Rep. SAND2018-5453C, Sandia National Laboratory, Livermore, CA, United States, 2018.
- [38] Jaravel, T., Labahn, J., Sforzo, B., Seitzman, J., and Ihme, M., "Numerical Study of the Ignition Behavior of a Post-Discharge Kernel in a Turbulent Stratified Crossflow," *Proceedings of the Combustion Institute*, Vol. 37, No. 4, 2019, pp. 5065–5072. https://doi.org/10.1016/j.proci.2018.06.226.
- [39] Tang, Y., Hassanaly, M., Raman, V., Sforzo, B., and Seitzman, J. M., "Numerical Simulation of Forced Ignition of Jet-Fuel/Air using Large Eddy Simulation (LES) and a Tabulation-Based Ignition," *57th AIAA Aerospace Sciences Meeting*, AIAA Paper 2019-2242, 2019. https://doi.org/10.2514/6.2019-2242.
- [40] Tang, Y., Hassanaly, M., Raman, V., Sforzo, B., and Seitzman, J., "Probabilistic Modeling of Forced Ignition of Alternative Jet Fuels," *Proceedings of the Combustion Institute*, 2020. https://doi.org/10.1016/j.proci.2020.06.309.
- [41] Als-Nielsen, J., and McMorrow, D., *Elements of Modern X-ray Physics*, John Wiley & Sons, Chichester (United Kingdom), 2011.
- [42] Richardson, E., and Mastorakos, E., "Numerical Investigation of Forced Ignition in Laminar Counterflow Non-Premixed Methane-Air Flames," Combustion Science and Technology, Vol. 179, No. 1-2, 2007, pp. 21–37. https://doi.org/10.1080/ 00102200600805892.
- [43] Maly, R., "Spark Ignition: Its Physics and Effect on the Internal Combustion Engine," *Fuel Economy*, Springer, 1984, pp. 91–148. https://doi.org/10.1007/978-1-4899-2277-9_3.
- [44] Kline, L. E., and Siambis, J. G., "Computer Simulation of Electrical Breakdown in Gases; Avalanche and Streamer Formation," *Physical Review A*, Vol. 5, No. 2, 1972, pp. 794–805. https://doi.org/10.1103/PhysRevA.5.794.

- [45] Zhang, W., Fisher, T., and Garimella, S., "Simulation of Ion Generation and Breakdown in Atmospheric Air," *Journal of Applied Physics*, Vol. 96, No. 11, 2004, pp. 6066–6072. https://doi.org/10.1063/1.1806264.
- [46] Kim, J., Gururajan, V., Scarcelli, R., Biswas, S., and Ekoto, I., "Modeling Nanosecond-Pulsed Spark Discharge and Flame Kernel Evolution," *Journal of Energy Resources Technology*, Vol. 144, No. 2, 2021, p. 022305. https://doi.org/10.1115/1.4051144.
- [47] Richards, K., Senecal, P., and Pomraning, E., "CONVERGE (Version 2.4.0) Manual," Tech. rep., Convergent Science, Inc., Madison, WI, United States, 2018.
- [48] Crespo-Anadon, J., Benito-Parejo, C. J., Richard, S., Riber, E., Cuenot, B., Strozzi, C., Sotton, J., and Bellenoue, M., "Experimental and LES Investigation of Ignition of a Spinning Combustion Technology Combustor under Relevant Operating Conditions," *Combustion and Flame*, Vol. 242, 2022, p. 112204. https://doi.org/10.1016/j.combustflame.2022.112204.
- [49] Sforzo, B. A., "High Energy Spark Ignition in Non-Premixed Flowing Combustors," Ph.D. thesis, Georgia Institute of Technology, Atlanta, 2014.
- [50] Gherardi, N., and Massines, F., "Mechanisms Controlling the Transition from Glow Silent Discharge to Streamer Discharge in Nitrogen," *IEEE Transactions on Plasma Science*, Vol. 29, No. 3, 2001, pp. 536–544. https://doi.org/10.1109/27.928953.
- [51] Akram, M., "Modelling of spark to ignition transition in gas mixtures," Ph.D. thesis, Lund Institute of Technology, Lund (Sweden), 1996.
- [52] McBride, B. J., Zehe, M. J., and Sanford, G., "NASA Glenn Coefficients for Calculating Thermodynamic Properties of Individual Species," NASA/TP—2002-211556, September, 2002.
- [53] Gombosi, T. I., and Gombosi, A., Gaskinetic theory, 9, Cambridge University Press, Cambridge (United Kingdom), 1994. https://doi.org/10.1017/CBO9780511524943.
- [54] Schulz, J., Gottiparthi, K., and Menon, S., "Ionization in Gaseous Detonation Waves," *Shock Waves*, Vol. 22, No. 6, 2012, pp. 579–590. https://doi.org/10.1007/s00193-012-0412-9.
- [55] Smith, G. P., Golden, D. M., Frenklach, M., Moriarty, N. W., Eiteneer, B., Goldenberg, M., Bowman, C. T., Hanson, R. K., Song, S., Gardiner, W. C. J., Lissianski, V. V., and Qin, Z., "GRI 3.0 Mech," 1999. URL http://combustion.berkeley.edu/gri-mech.
- [56] Goodwin, D. G., Moffat, H. K., and Speth, R. L., "Cantera: An Object-Oriented Software Toolkit for Chemical Kinetics, Thermodynamics, and Transport Processes, Ver. 2.2.1," 2017. URL https://cantera.org/documentation/.
- [57] Pischinger, S., and Heywood, J. B., "How Heat Losses to the Spark Plug Electrodes Affect Flame Kernel Development in an SI-Engine," *SAE Transactions*, 1990, pp. 53–73. https://doi.org/10.4271/900021.
- [58] Grosshandler, W. L., "RADCAL: a Narrow-band Model for Radiation," Calculations in a Combustion Environment, NIST Technical Note, Vol. 1402, 1993.

- [59] Kabbaj, N., Cressault, Y., Teulet, P., Reichert, F., and Petchanka, A., "Numerical Optimization of Mean Absorption Coefficient in Air using Planck Modified Mean Function," *Journal of Physics: Conference Series*, Vol. 1243, IOP Publishing, 2019, p. 012015. https://doi.org/10.1088/1742-6596/1243/1/012015.
- [60] Pope, S. B., "Ten Questions Concerning the Large-Eddy Simulation of Turbulent Flows," *New Journal of Physics*, Vol. 6, No. 1, 2004, p. 35. https://doi.org/10.1088/1367-2630/6/1/035.
- [61] Germano, M., "Turbulence: the Filtering Approach," *Journal of Fluid Mechanics*, Vol. 238, No. 1, 1992, pp. 325–336. https://doi.org/10.1017/S0022112092001733.
- [62] Senecal, P., Pomraning, E., Richards, K., Briggs, T., Choi, C., McDavid, R., and Patterson, M., "Multi-Dimensional Modeling of Direct-Injection Diesel Spray Liquid Length and Flame Lift-off Length using CFD and Parallel Detailed Chemistry," SAE Transactions, 2003, pp. 1331–1351. https://doi.org/10.4271/2003-01-1043.
- [63] Issa, R. I., "Solution of the Implicitly Discretised Fluid Flow Equations by Operator-Splitting," *Journal of Computational Physics*, Vol. 62, No. 1, 1986, pp. 40–65. https://doi.org/10.1016/0021-9991(86)90099-9.
- [64] Van Leer, B., "Towards the Ultimate Conservative Difference Scheme. V. A Second-Order Sequel to Godunov's Method," *Journal of computational Physics*, Vol. 32, No. 1, 1979, pp. 101–136. https://doi.org/10.1016/0021-9991(79)90145-1.
- [65] Pal, P., Kumar, G., Drennan, S. A., Rankin, B. A., and Som, S., "Multidimensional Numerical Modeling of Combustion Dynamics in a Non-Premixed Rotating Detonation Engine With Adaptive Mesh Refinement," *Journal of Energy Resources Technology*, Vol. 143, No. 11, 2021. https://doi.org/10.1115/1.4050590.
- [66] Kastengren, A., Duke, D., Swantek, A., Sevik, J., Matusik, K., Wallner, T., and Powell, C. F., "Time-resolved X-ray Radiography of Spark Ignition Plasma," SAE International Journal of Engines, Vol. 9, No. 2, 2016, pp. 693–703. https://doi.org/10.4271/2016-01-0640.